

Table of Contents

1.0	Introduction
1.1	Technical Requirements
2.0	Planetary Science
2.1	Atmospheric Model of Mars
2.2	Soil study
2.3	Landing Site Selection
3.0	Avionics
3.1	Flight Hardware
3.2	UAV Circuit Model
3.3	Man Machine Interface Model
3.4	Wireless Communication System
4.0	Materials
5.0	Propulsion
5.1	Propulsion Subsystem
5.2	Computational Fluid Dynamics
5.3	Structural Analysis
5.4	Final Geometry
5.5	Swash Plate
6.0	Structures
6.1	Frame
6.2	Pickup mechanism of UAV
7.0	Epilogue
8.0	Future Advancements
9.0	References
10.0	Appendix

1. Introduction

The avionics systems of our **Unmanned Aerial Vehicle (UAV)** have been designed with hardware and software having equal importance. Our design aims to address various challenges faced by small UAV systems, such as navigating through rough terrain, wind disturbance, power control, system integration, etc.

1.1. Technical Requirements

The technical specifications of the UAV or its required capabilities are shown in Figure 1.1.

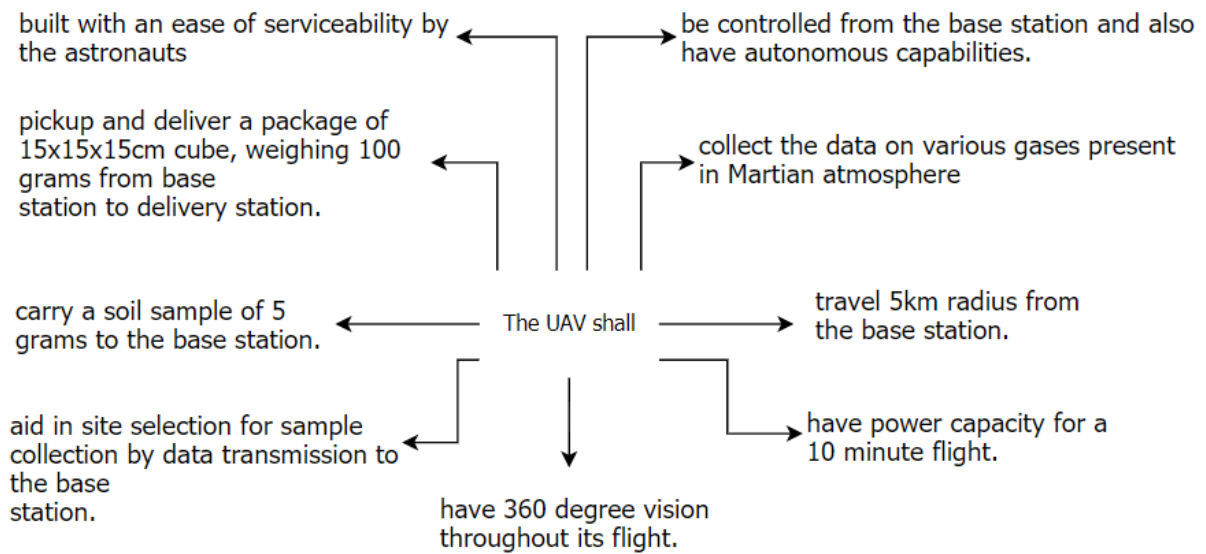


Figure 1.1 UAV Capabilities

The orthographic labelled view of the UAV is shown in Figure 1.2

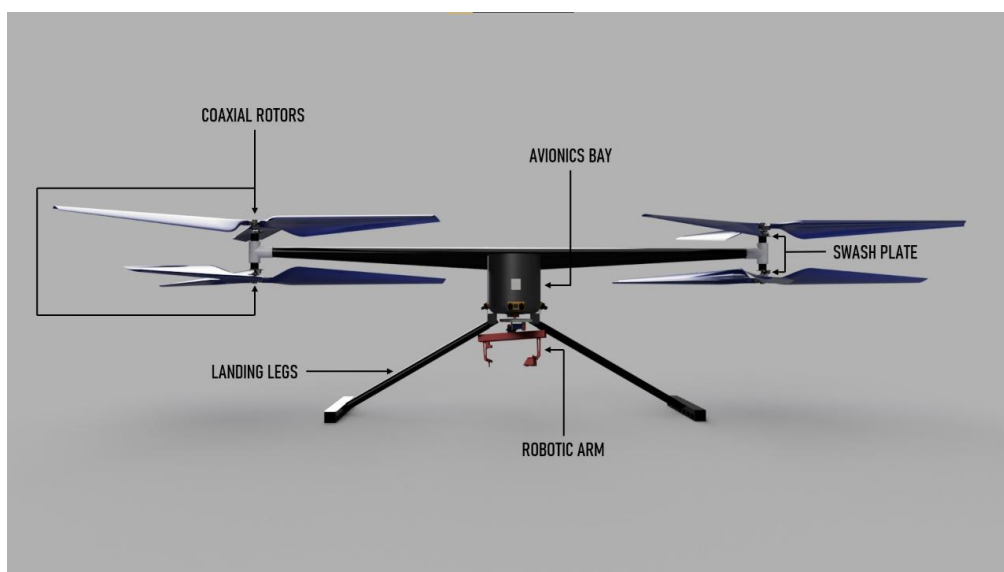


Figure 1.2 Labelled and Orthographic view of the UAV

2. Planetary Science

2.1. Atmospheric Model of Mars

Mars' atmosphere is composed primarily of carbon dioxide (about 96 percent), with minor amounts of other gases such as argon and nitrogen. The atmosphere is very thin and the atmospheric pressure at the surface of Mars is only about 0.6 percent of Earth's (101,000 pascals). Scientists think that Mars may have had a thicker atmosphere early in its history, and data from NASA spacecraft (the MAVEN mission) indicate that Mars has lost significant amounts of its atmosphere through time. The primary culprit for Mars' atmospheric loss is the solar wind!

The six most common components of the atmosphere are listed out in Table 2.1.

Table 2.1: Atmospheric Composition		
Carbon dioxide (CO ₂): 95.32%	Nitrogen (N ₂): 2.7%	Argon (Ar): 1.6%
Oxygen (O ₂): 0.13%	Water (H ₂ O): 0.03%	Neon (Ne): 0.00025%

Martian air contains only about 1/1,000 as much water as our air, but even this small amount can condense out, forming clouds that ride high in the atmosphere or swirl around the slopes of towering volcanoes. Local patches of early morning fog can form in valleys. At the Viking Lander 2 site, a thin layer of water frost covered the ground each winter. There is evidence that in the past a denser Martian atmosphere may have allowed water to flow on the planet. Physical features closely resembling shorelines, gorges, riverbeds and islands suggest that great rivers once marked the planet.

Atmospheric Modelling: Mars GRAM 2010 was used for atmospheric modelling of Martian surface and temperature, pressure, density and albedo was thoroughly analysed. Graphs were plotted showing variation of each of the above-mentioned parameters with latitude and solar longitude (position of the sun on the celestial sphere along the ecliptic).

Temperature and Pressure

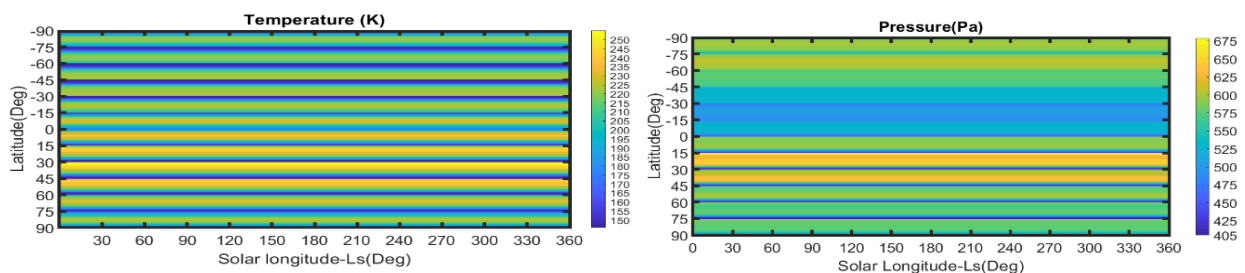


Figure 2.1 Temperature and Pressure Scales

The average recorded temperature on Mars is -63°C (-81°F) with a maximum temperature of 20°C (68°F) and a minimum of -140°C (-220°F).

Barometric pressure varies at each landing site on a semi-annual basis. When the southern cap was largest, the mean daily pressure observed by Viking Lander 1 was as low as 6.8 millibars; at other times of the year, it was as high as 9.0 millibars. The pressures at the Viking Lander 2 site were 7.3 and 10.8 millibars. In comparison, the average pressure of the Earth is 1000 millibars.

Density

The density of the atmosphere varies seasonally, as winter forces carbon dioxide to freeze out of the Martian air. In the ancient past, the atmosphere was likely thicker and able to support water flowing on its surface. Over time, lighter molecules in the Martian atmosphere escaped under pressure from the solar wind, which affected the atmosphere because Mars does not have a global magnetic field.

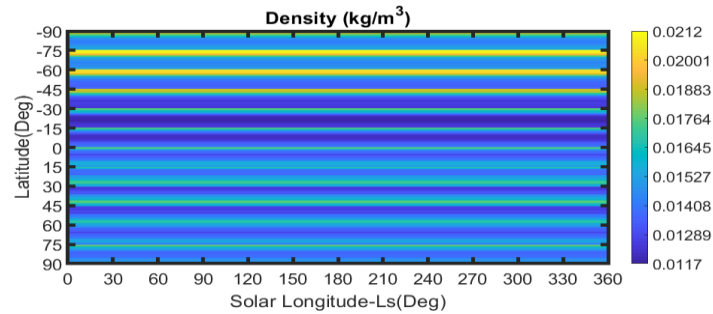


Figure 2.2 Density Scale

Albedo

The albedo of any planetary surface is defined as the fraction of incident solar radiation reflected by the surface. The magnitude and spatial distribution of Martian surface albedo are important inputs for characterisation of Martian surface and Atmospheric circulation. In general, low albedo values are associated with a darker surface on Mars having volcanic rock basalt on the surface. Higher albedo values represent surfaces covered by Dust. The area shown in blue colour indicates the presence of basaltic composition while yellow indicates the dust covered regions of Mars.

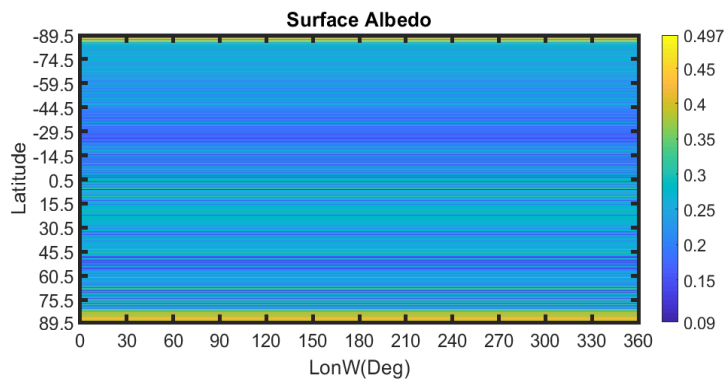


Figure 2.3 Surface Albedo Scale

Magnetic field

Mars, contrary to Earth does not have a major global magnetic field due to the non-existence of inner dynamo that is the source of magnetic fields on our planet. Dynamo theory describes the process through which a rotating, convecting, and electrically conducting fluid acts to maintain a magnetic field, explaining the presence of magnetic fields in astrophysical bodies. However, Mars has a magnetosphere much simpler and less extensive than Earth's, but the red planet does not have a magnetic field shield preventing charged particles from reaching the planet surface, like the solar wind. The particles borne by the solar wind through the Solar System are typically electrically charged. Their interaction forms the magnetosphere from magnetic field tubes, posing challenges for mitigating solar radiation and retaining an atmosphere. The solar wind carries magnetic field lines from the Sun that drape themselves around the planet, once they cannot pass through electrically conductive bodies like Mars.

The primary hindrance to the solar wind is the electrically charged region in its upper atmosphere, ionosphere. Due to Mars' small size, mass and gravity there is an extended exosphere that is the outermost layer of the atmosphere (where molecules meet outer space and solar winds).

In addition to, this planet is half magnetised as there is major contrast in elevation between the southern highlands and northern lowlands, the elastic part of the crust is thinner in the north than it is in the south where there is more exhuming. Other aspects important to take in consideration when studying magnetism in Mars is the presence of a Magnetic Pileup Boundary and Photo-Electron Boundary.

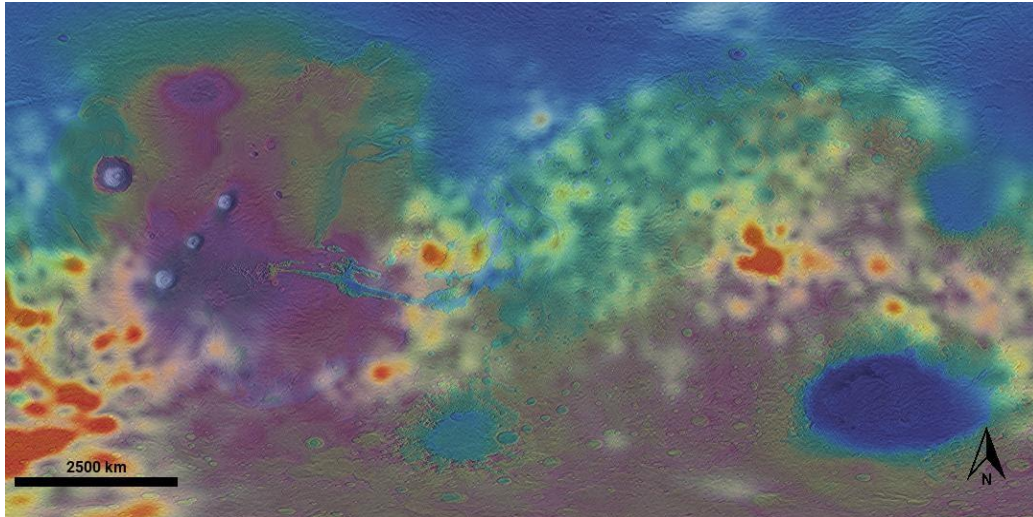


Figure 2.4 Fig: Following figure shows a magnetic field (magnitude only) map overlaid on the Martian map. Active magnetic regions are in red. This was created in JMARS GIS software. [6]

2.2. Soil Study

Topography

In order to choose a landing site for the UAV it is essential to have in-depth knowledge of topography of the Martian surface (some features studied in Appendix B). The surface of Mars can be divided into northern plains, southern highlands and the Tharsis plateau. So far it is observed that the northern hemisphere of the planet is much lower, comparatively flat and uniform compared to the southern hemisphere of the planet. The southern hemisphere is covered with enormous craters. The Tharsis plateau has shown to have major tectonic activities in the past and is a huge volcanic province.

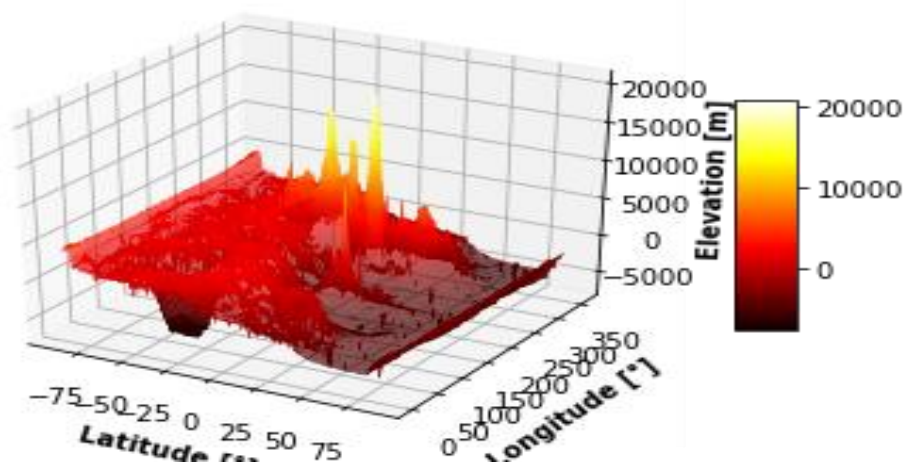


Figure 2.5 Fig: Martian topography as simulated in python with real data from Mars GRAM 2010.

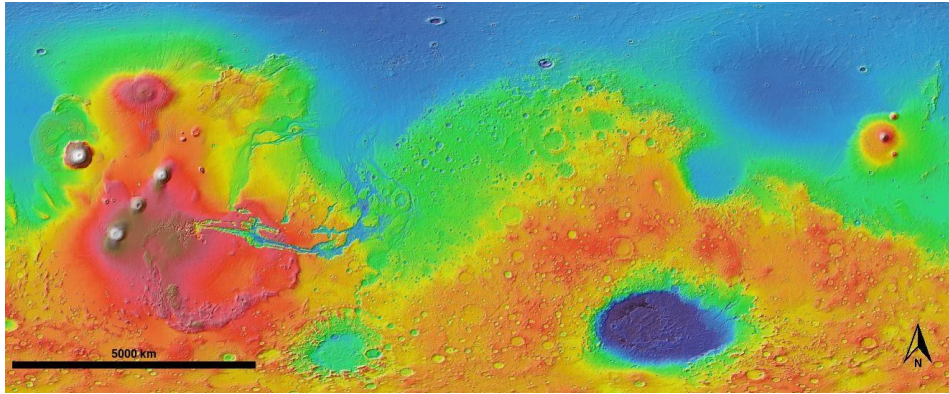


Figure 2.6 2D elevation image colour image, showing entire Martian surface created in JMARS GIS. [7]

2.3.2. Soil composition and tectonics

Martian Soil is almost entirely made up of mineral matter (silicon, oxygen, iron, magnesium, aluminium, calcium and potassium are the most abundant elements available in the Martian crust, refer appendix A), with small amounts of water. The mineral matter present in Martian soil comes from weathered volcanic rocks. It is overall a sandy soil along with a thin surface layer of very small (generally 3 μm in diameter) dust particles. The soil has a red/orange colour because it contains plenty (5 to 14 percent) of iron oxides (nanophase Iron (III) Oxide). It is like iron-rich volcanic soils on Earth. In contrast to Earth, the soil on Mars is relatively homogenous (the same everywhere), since global dust storms move the soil around the planet. [1]

Containing just 2% water, Mars is extremely dry. The average temperature of Mars is too cold to support liquid water at the surface, but salts present in the soil drop its freezing point, hence allowing briny films to form. Life is difficult to sustain in Mars's extreme cold temperatures. Sunlight and heat reaching that planet is much less as compared to what the Earth gets. This is because Mars is roughly 50 million miles farther away from the Sun. In addition to it the Martian atmosphere is too thin to keep our planet warm. [2][3]

Mars' crust is thought to be one piece. That doesn't mean the crust sits quietly. According to a new research powerful landslide may speed down Martian slopes at up to 450 mph (725 km/h). [4]. Two strong, clear quakes have been detected by NASA's InSight lander, originating in a location of Mars called Cerberus Fossae (the same place where two strong quakes were seen earlier in the mission). InSight has recorded over 500 quakes to date.

2.3. Landing Site Selection

1. A suitable site for the UAV will be in a lower lying area where **atmospheric density** is comparatively **higher** for optimum thrust.
2. Mid-latitudes have **higher temperature** all year around as compared to higher latitudes thus suitable to power the rover and less load will be on the heating/thermal system when the temperature falls below zero at night. Poles will not be a suitable landing site as temperature at poles drops to around -160° Celsius in winters.
3. To help the rover in **smooth landing** a fairly uniform plain/flat land is preferred.
4. Few **more parameters** such as radiation received, magnetic field components, coronal mass ejections, diurnal and seasonal temperature and pressure changes, dust storms and presence of life need to be also considered while selecting a landing site.

- Other than from an engineering perspective, it is essential from a **scientific research** aspect to find a landing site which has rocks and soils that could have supported **life** (refer Appendix C) in ancient times, or if the landing site was a **water/ ice** source or has a water bearing mineral.

Considering above parameters, considerable ranges of these parameters were discussed with other subsystems and by simulating known data for different martian regions (Appendix D) Jezero Crater was chosen as the most suitable site for UAV landing and astronaut assistance. Jezero specifications are given below in Table 2.2.

Latitude	Longitude	Temperature
18.38°N	77.58°E	Surface: 185 K - 285 K, air: (14.5m) - 195 K - 250
Pressure	Density	Wind Speed
640 - 820 Pa	7.11×10^{-3} to 8.18×10^{-3} kg/cu m	0 to 15 m/s

3. UAV Avionics

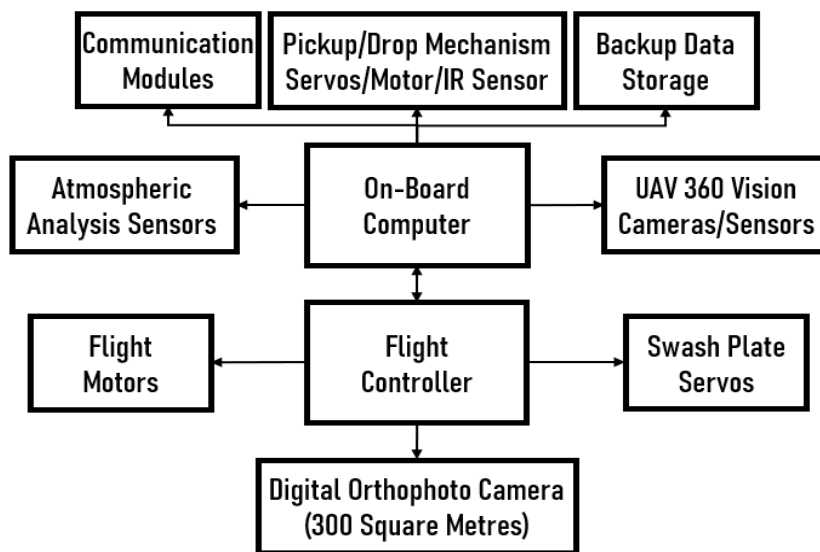


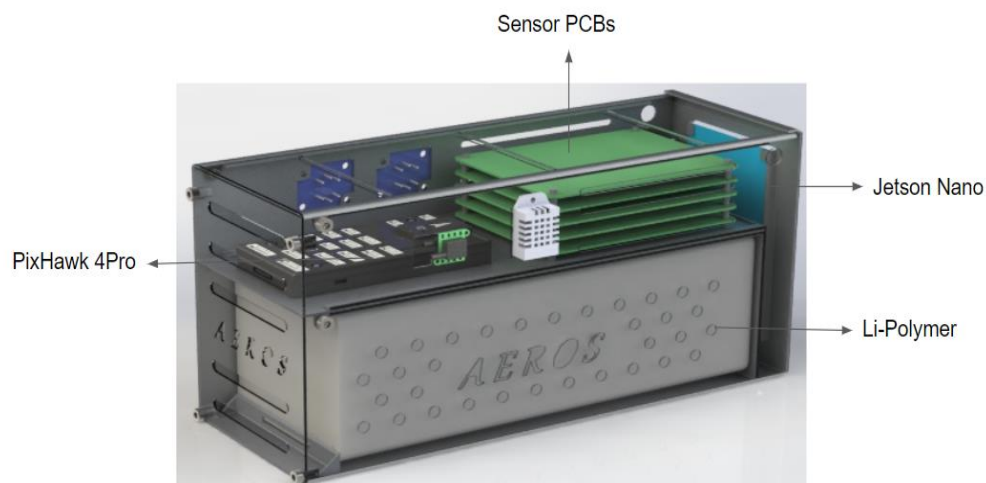
Figure 3.1. UAV Flight Hardware Architecture

3.1. Flight Hardware

Jetson nano: The main system processor that handles all the path planning algorithms and image processing onboard. The computer along with a flight controller lets the UAV do the tasks it is designed to.

- Pixhawk 4:** This STM32 microcontroller-based flight computer is the reason the UAV can remain in the air. It handles all the crucial calculations and control signals required to keep it in the air.
- PX4 optical flow camera:** The camera works alongside the main system cameras to generate an orthophoto, being a flow-based camera, it can handle inframe translation effectively while still being able to capture a steady photograph.

3. **3D blackbird camera:** The camera when paired up with 2 more is used in the flight stack to generate the 360⁰ photographs by taking all the individual images and matching their features and stitching them together by matching their contours.
4. **Thin-film cryogenic temperature sensor:** At cryogenic temperatures, a semiconductor-based temperature sensor is inaccurate and is hence unreliable. Therefore a resistance-based cryogenic temperature sensor handles temperatures very well due to its simplistic design and can also remain accurate at ranges from 0.1 K up to 420 K.
5. **Atmospheric Gas sensor:** Analysing the atmospheric conditions besides temperature only is handled by this sensor. The sensor has a pretty wide detection scope so a single sensor is enough to measure the presence and composition of multiple gases like CO₂, NO, Argon and NH₃.
6. **Garmin LIDAR sensor:** For surface contour detection and navigation based on these features, the LIDAR is a perfect choice as LIDAR is a prime technique in mapping. The generated map and mesh are used for navigation close to the surface where the camera data is not accurate enough.
7. **Main flight motor EC-4 pole:** Maxon drive brushless motors to have a good working temperature range and since they have been used on previous mars missions, the choice was obvious. These motors are mainly brushless in runner type and expose as little of their bearings and coils to the harsh elements of the Martian atmosphere hence increasing reliability and longevity on the rotor.
8. **Swashplate motor DCX 10 S:** These brushed motors made by Maxon again are brushed type DC motors with a nominal torque of 0.95 Nm at 12 V and the brushes are made of precious metals hence providing a high-quality reliable swashplate design for the rotors.
9. **Arm actuator flat motor:** This particular motor is a brushless 15 W motor with the ability to be used with a hall sensor which can help in accurate position detection and closed-loop control. These motors are also outfitted with a planetary gearbox for increased torque and reduced RPM making them the ideal choice for actuator motors.
10. **Electronic Speed controller**
11. **Kaplan Heating element:** This is placed on the surface of the avionics bay, it activates when the temperature limit drops below 5⁰ Celsius.
12. **Pressure & Humidity Sensor:** It is primarily used for temperature compensation of the it, and can also be used for estimating ambient temperature.
13. **Other Essential Sensors:** shown below



14. **Power Supply :**13000 mA Li Polymer battery.

Figure 3.2

System Architecture of Autonomous Mars UAV

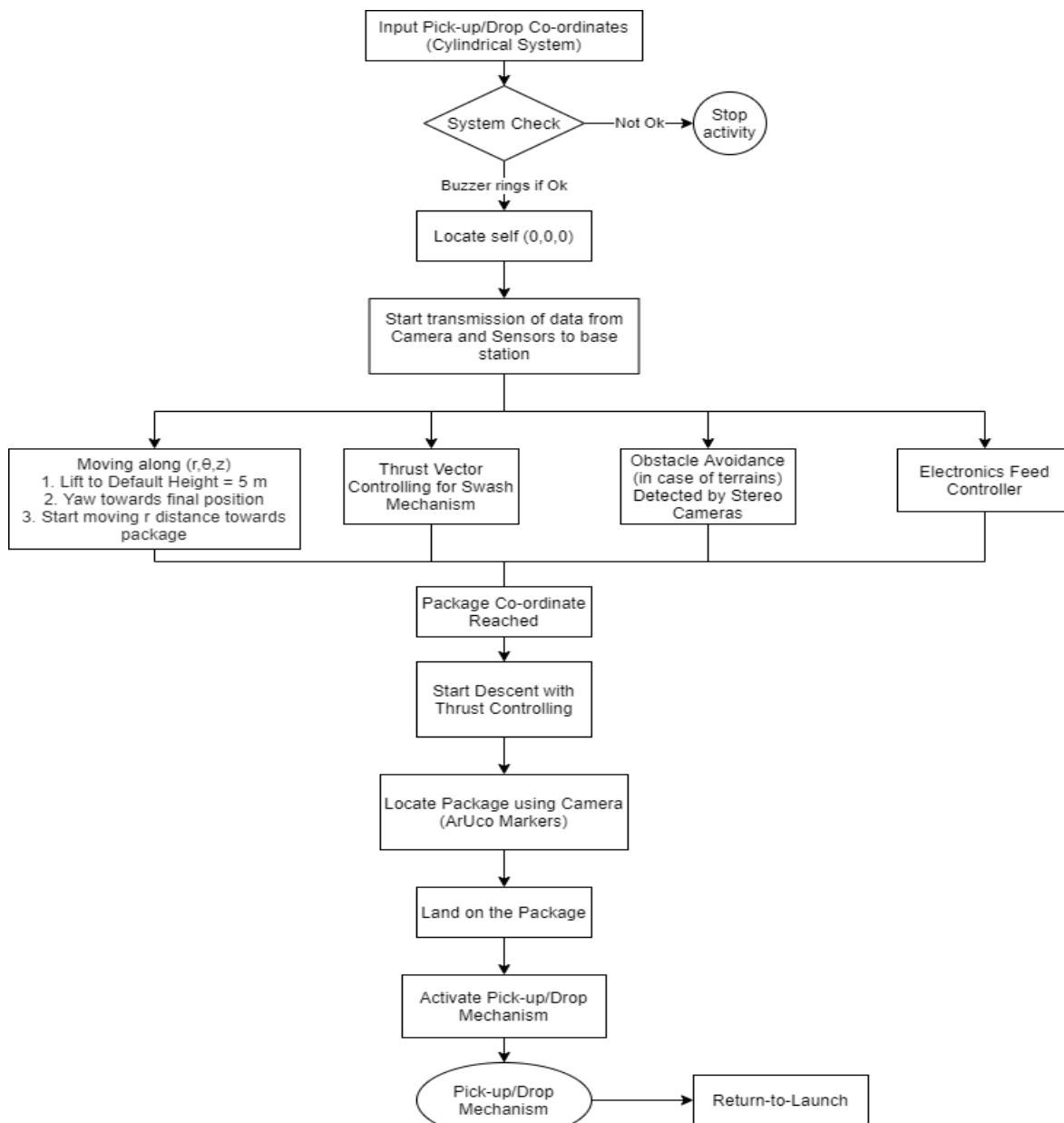


Fig 3.3: System flow diagram

In the above flowchart, the general flow of the system has been discussed. The UAV is capable of up to 10 minutes of mission flight time along with collecting, carrying, and dropping the payload at specified locations in a cylindrical coordinate system that is of 5 kms in radius. The cylindrical system is so designed around the base station that a given location in the 5 km area can be depicted as an (r, θ, z) coordinate system to which the path is planned and that path is followed by the UAV. The multiple cameras and sensors on the flight computer allow for precise path planning, following, and execution in case of an obstacle being detected in the path. They have cameras that allow 360° photographs along with an orthographic picture along with their primary functions of path planning, obstacle detection, and object detection. At any point of time if any anomaly occurs with the UAV, Man Machine Interface (MMI) has a Return To Launch site (RTL) push button which overrides the UAV to returns to the base/astronaut.

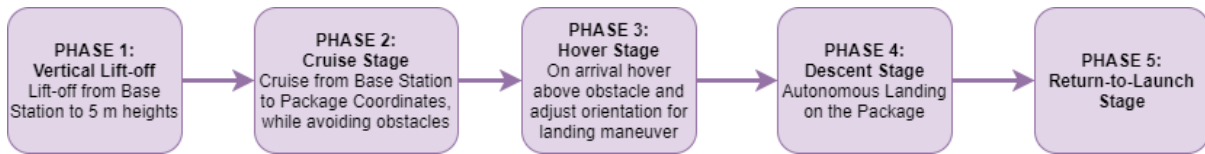


Figure 3.4: Physical Electronics System

3.2. UAV Circuit Model

Several factors are crucial for small unmanned aircraft. They can be loosely broken down into four categories: propulsion, light-weight pickup and frame structures, aerodynamic performance, and avionics system design and integration. The last of these includes sensors, communications, algorithms, and firmware, which are considered below for the application of Mars UAV. The circuit model is shown in Figure 3.5.

3.3. Man Machine Interface Model

Ground control station is a UAV ground control terminal, the hardware system includes equipment boxes, panels, and internal support structure, host computer system, auxiliary control computer systems, wireless data transmission link, wireless image transmission links, power systems, built-in remote-control system.

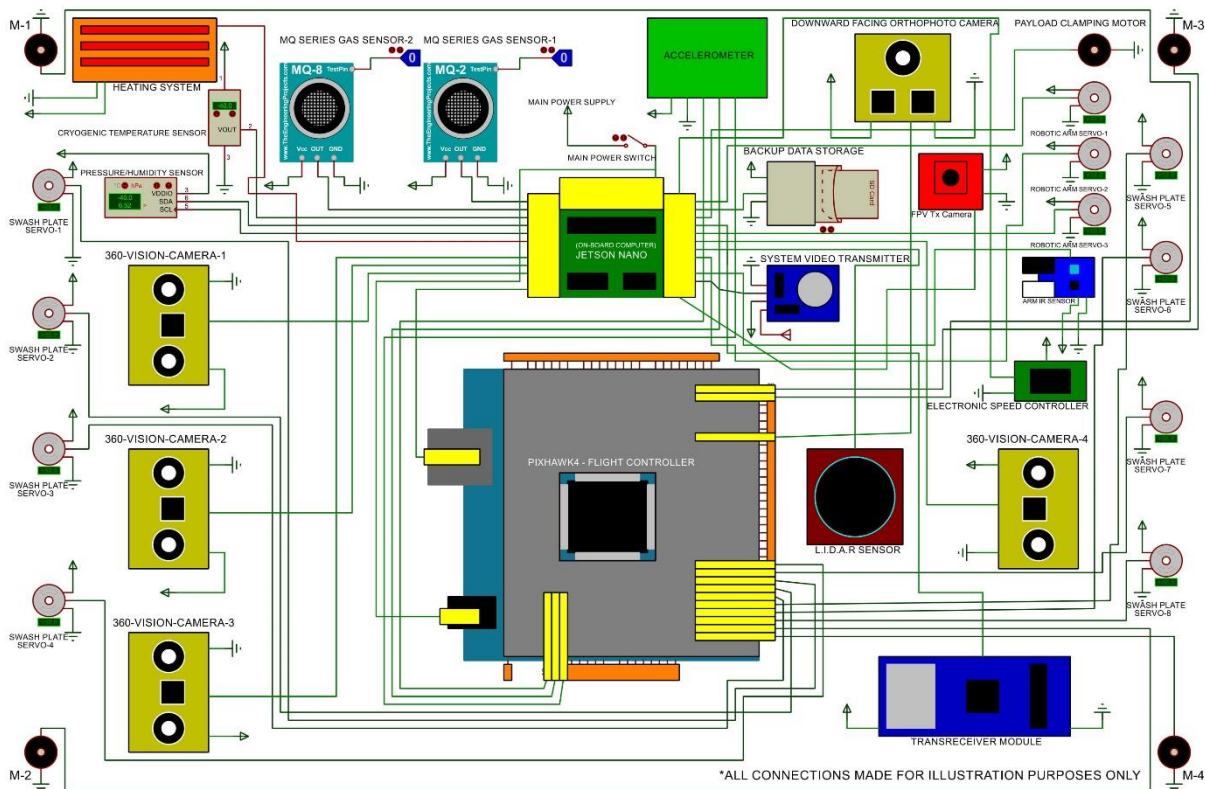


Figure 3.5: UAV Circuit Model

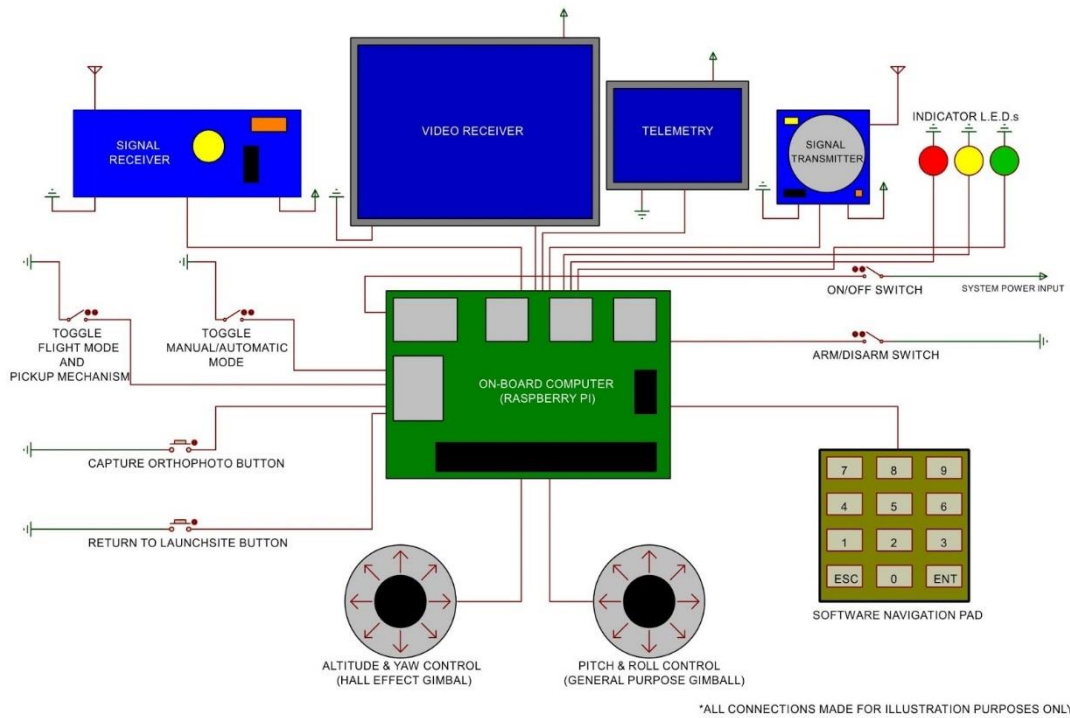


Figure 3.6: Guidance, Navigation and Stability Control System

Table 3.1: Sensors used for self-localisation and path planning		
Sensors	Purpose	Uses in GNC
Garmin lidar lite v3	Mapping	Used for navigation and collision avoidance by UAVs
PX4FLOW Smart Camera OR Pro	Orthophoto	To create extremely detailed and accurate maps. Large quantities of images are taken during a drone flight, the scale is kept constant and the images are referenced to ground control points.
3D Blackbird camera X 4	360 vision	To capture real time videos and pictures during navigation
PX 4 Pro	F.C	To detect movement of the drone, as well as user commands. Using this data, it then controls the speed of the motors to make the craft move as instructed.

3.3.1. Flight Dynamics Model

Dynamic Inversion approach will be used for controlling position and orientation of the vehicle. Rotation dynamics is faster than translation dynamics is faster than translation dynamics., therefore time scale

separation principle will be used. Second order stable error dynamics will be used where x denotes the State Vector.

$$\ddot{e} + 2\xi\omega_n\dot{e} + e = 0 \quad e = x - x_d$$

$$\omega_{n_{Rotation}} > \omega_{n_{Translation}}$$

$$\xi = 0.7 - 0.9$$

3.3.2. Path Planning Model

Stereo Image pairs (Lt, Rt), (Lt+1, Rt+1) at time T and T+1 are taken and processed to compensate lens distortion, stereo rectification to obtain parallel epipolar lines. Features in (Lt) image are detected by FAST corner detector and tracked in (Rt) by Kanade-Lucas-Tomasi optical flow tracker (15x15 search window, 3 image pyramid level). Perform outlier rejection methods (RANSAC) over the matches for accuracy. Compute 3D point clouds by Triangulating image pairs. Pose estimation algorithm (Perspective n-Point) is performed over 3D point cloud and corresponding feature matches to obtain Rotation and Translation matrix. Reprojection error is minimized using Bundled adjustment. Decomposition of Rotation and translation matrix, Inertial measurement unit (IMU) data are processed through EKF (Extended Kalman Filter) to give control inputs (yaw, pitch, roll, translation).

3.3.3. Terrain Obstacle Avoidance Model

Obstacle avoidance is performed using cameras which detect obstacles using deep learning algorithms (like YOLO) and classify their type. If an obstacle is detected, the drone will fly sideways to avoid the obstacle and return to the obstacle detection state to check if there is an obstacle in the front before starting to fly straight forward otherwise repeat the process till no obstacle is detected. Deviation during the process is computed and control signals are modified after avoidance comparing ground truth. [8]

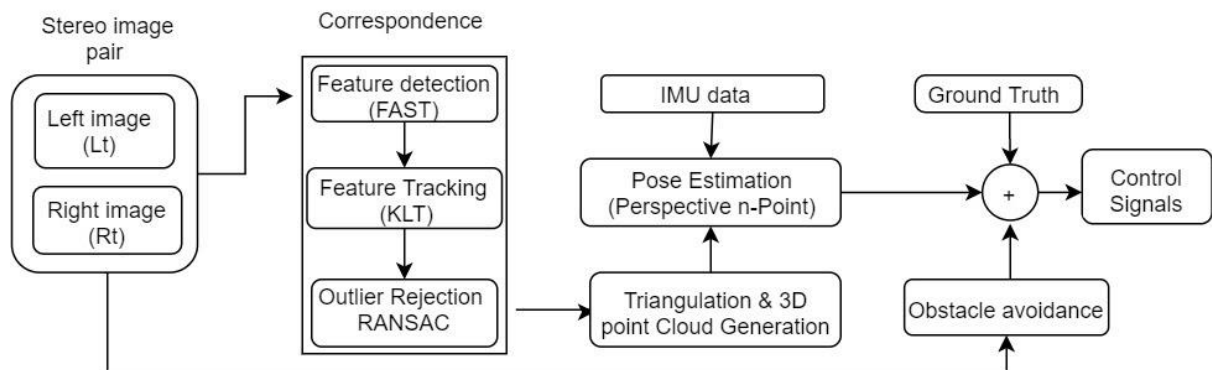


Figure 3.7 Navigation and path planning

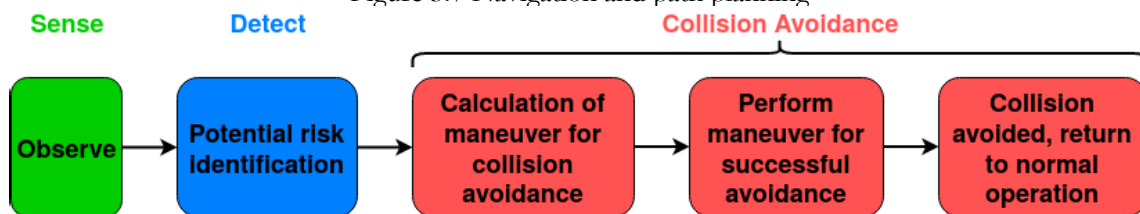


Figure 3.7 Obstacle Avoidance Model

3.3.4. Advanced Terrain Analysis For Navigation

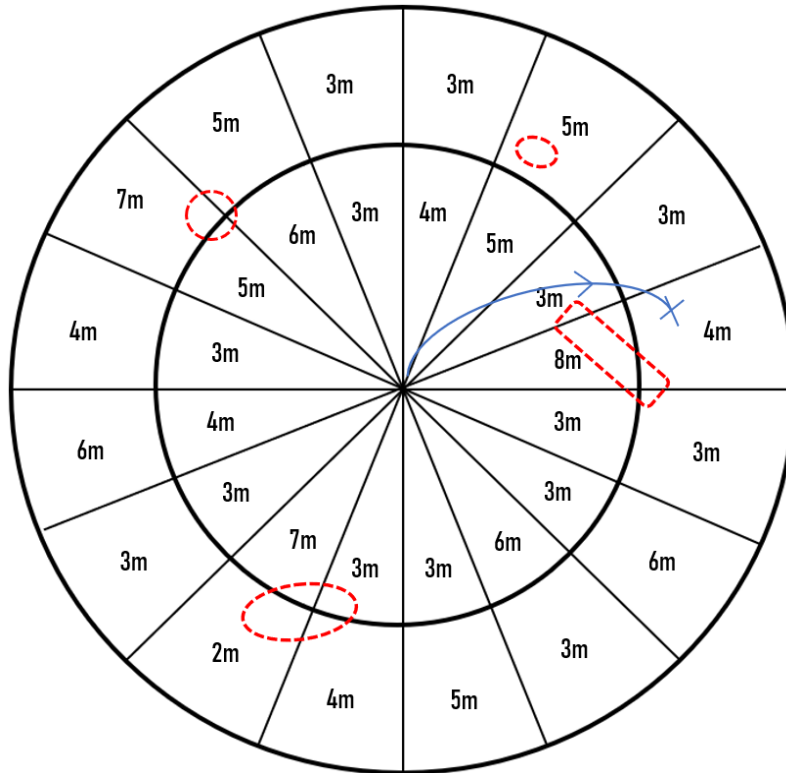


Figure 3.8: 5 km radius Terrain Model

Despite being equipped with obstacle avoidance functionalities, we have developed an algorithm that allows our UAV to navigate itself through the region (5km radius) while being quicker and safer. The red planet has a very rocky terrain with unpredictable changes in the surface below. Therefore, to fly on the red planet at high speeds with maximum reliability, it is imperative for the UAV to already know the surroundings to a certain extent. This reduces the need for abrupt obstacle avoidance (potentially put the craft in harm's way) and allows the UAV to reach its destination faster.

Our Algorithm uses real orbiter data (Using the Software: Jmars) to analyse the region around our base station and create a grid (Consisting of 32 sections - example shown in Figure 3.8) with each section having an average altitude value that the UAV will attain when travelling in that region to reduce abrupt changes in altitude and move at a faster speed. This system also marks regions that the UAV should avoid at all times in flight (Regions of steep depressions or mountains - Marked in Red inside figure), this means that the UAV will be able to map out the safest route to its destination right at take-off. This allows the UAV to seamlessly change altitude according to the grid it is in and avoid regions with extreme terrain, which in turn reduces its flight time, while increasing safety.

3.3.5. Package Detection Model

“ArUco” markers have been employed and the neighbourhood border/contour tracing algorithm of Suzuki in the OpenCV library is proposed to be used for this purpose. The returned value of this method will be a list of quadrilaterals and each quadrilateral describes a contour. After removing the contours containing areas less than one-fifth of our image columns, the threshold of the detected area will be calculated again using Otsu’s algorithm, to obtain a better quality. A standard ArUco marker can be seen as a 7×7 binary matrix, with each row of inner 5×5 matrices consisting of 2 bits of data and 3 bits of

fault detection. This matrix produces a 10-bit code, enabling us to detect 1024 different markers. Finally, the errors of these codes can be calculated to find the appropriate rotation, after which, corners of the markers are expected to have a proper amount of accuracy which can be evaluated with the help of the corner Subpixel function OpenCV library. The landing and pickup procedure will be followed after this. [9]

3.4. Wireless Communication System

Testing for wireless communication systems in relevant environments is far more complicated for Mars UAV than for typical Earth-Based UAV. Mav-Link protocol Communication is established during the entire critical phases of flight, that is Take-off & Landing between the Unmanned Aerial Vehicle and Martian Base. The Non-LOS link is achieved by patch antenna on UAV, the helicoidal antenna on portable control station MMI and parabolic dish transceiver tracking antenna at the Ground station. Wireless Communication is established with UAV based upon 3 cases of typical use:

Case1. UAV-aided ubiquitous coverage

Case2. UAV-aided relaying

Case3. UAV-aided information, collection / package delivery, dissemination / data



Figure 3.9: Conceptual Model

3.4.1 Conceptual Model

The proposed engineering model is enabled by harvesting wireless technology in UAV & establishes Energy-efficient communication via Mav-Link for case 3 typical usage scenario and a man machine



interface for initiation. Two-way Connections of ground-to-air & air-to-ground are Supported from this design for coverage enhancement and to enable fast, flexible, and efficient deployment in emergencies and package delivery at precise location within the 5km radius from base station with a tracking parabolic dish antenna. Localization and information dissemination are done throughout the flight and is relayed to portable MMI in the same radius of Ground station.

Figure 3.10: MMI

3.4.1. System Flow Algorithm

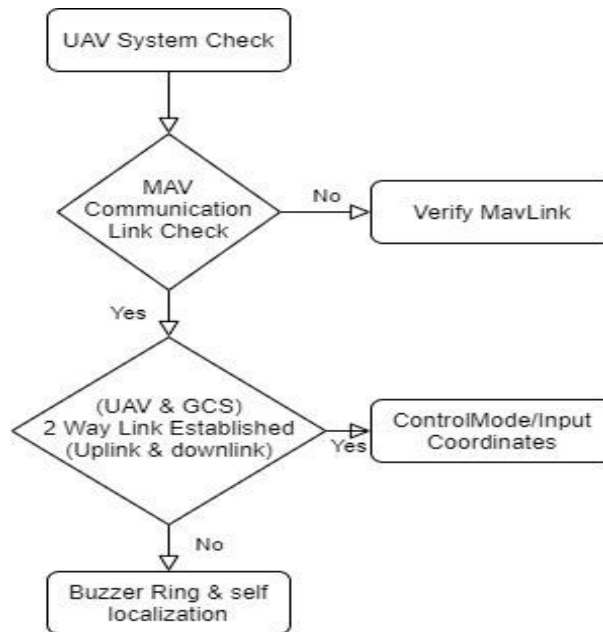


Figure 3.10: System Flow Algorithm

The communication link flow diagram shows the two-way connection interface of Martian Base Ground Control Station (GCS) and Unmanned Aerial Vehicle (UAV) is achieved by MavLink Protocol. It can also be piloted using a portable Man Machine Interface (MMI).

3.4.2. Mars GCS & UAV Link Characteristics

Main Channel - MAV, MMI, GCS

UAV Uplink - Patch Antenna

UAV VideoTx - Clover leaf Antenna

Base Station Downlink/Uplink - UHF Parabolic Dish Antenna

Man, Machine Interface Uplink - Dipole Antenna

Telemetry/Video Downlink - Helical Antenna

Characteristics - QPSK Modulator with 5 dB Attenuation

Link Margin - 39.45 dB

Data Rate(Uplink/Downlink) - 10 Mbps

Range - Upto 10 Km Diameter

Energy Required - 5 Watts

4. Materials

Unlike materials used in UAV on earth, for Martian atmosphere the materials are selected on basis of their mechanical strength, survivability, radiation handling capacity and withstand freezing low temperatures. Below are few listed materials which are used in our UAV for mars atmosphere. The materials used in various parts of the UAV are shown in Figure 4.1 – 4.6.

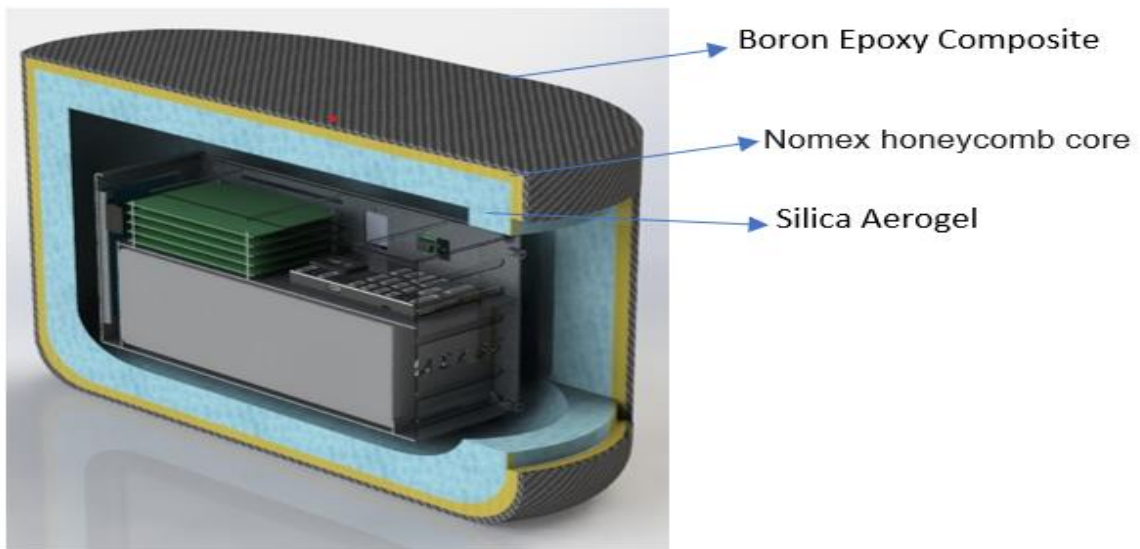


Figure 4.1: Avionics Bay – Thermal Layers

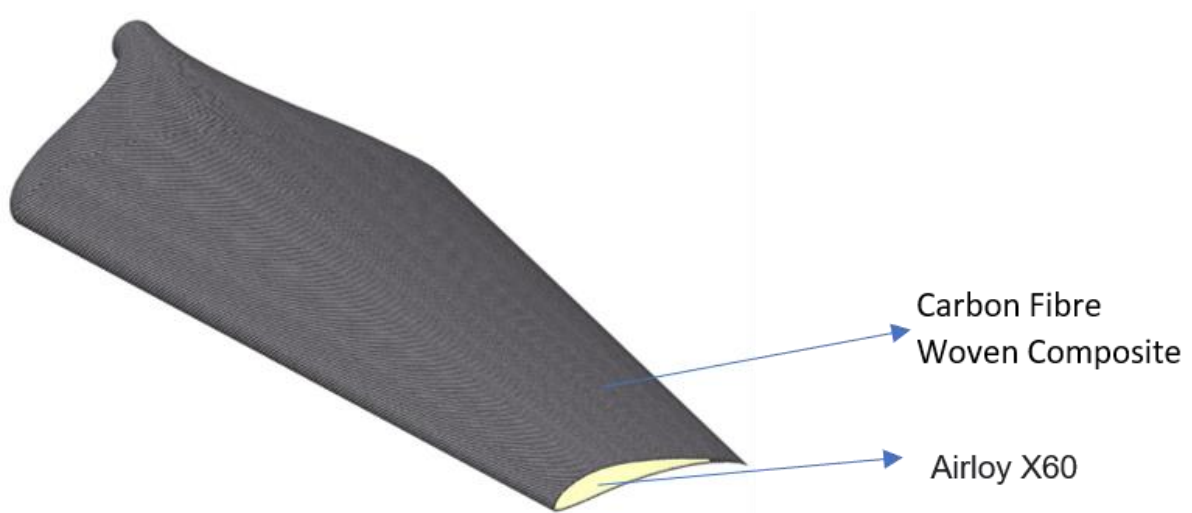


Figure 4.2: Blade Cross Sectional View



Figure 4.3: Frame supporting rotors and housing for avionics bay

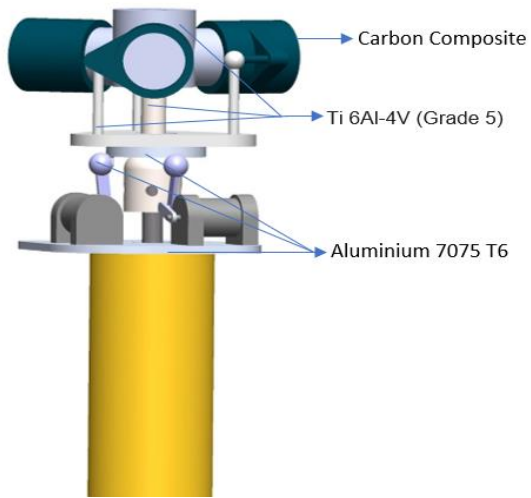


Figure 4.4: Swash Plate Materials

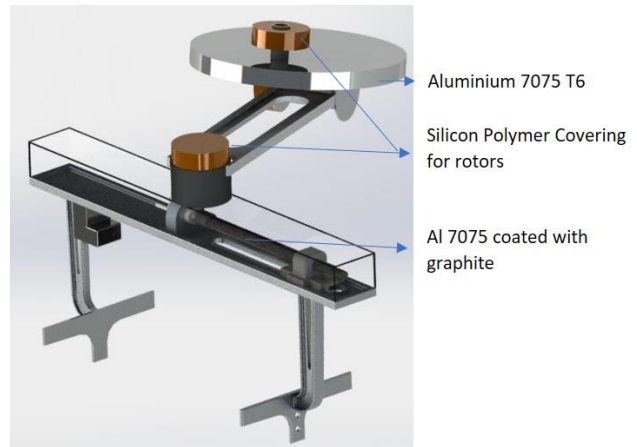


Figure 4.5: Pickup Mechanism Materials

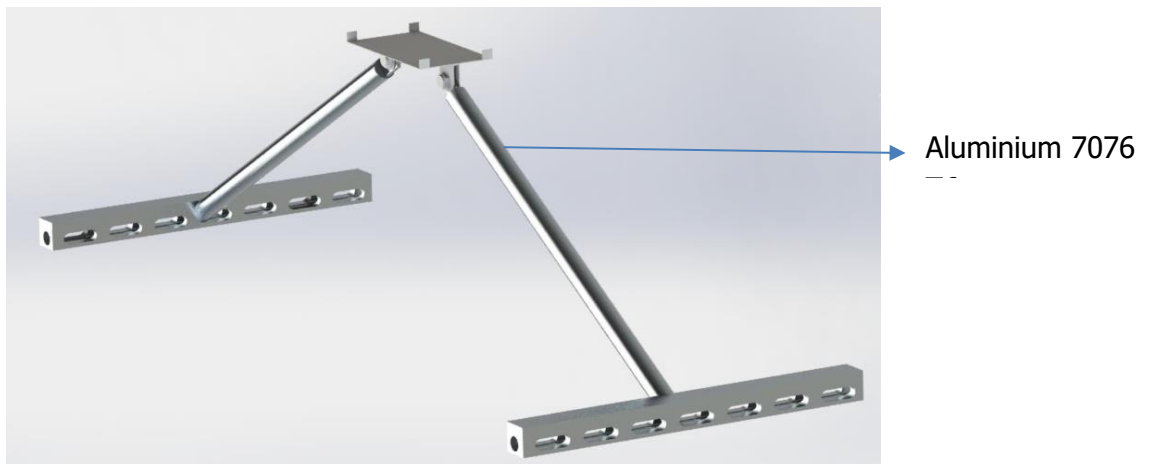


Figure 4.6: UAV Supporting Base Material

For further information please refer to the Appendix C (materials) for appropriate values.

5. Propulsion

5.1. Propulsion Subsystem

The requirement for the propulsion system was that it should be capable of lifting a weight of almost 8.5 kg based on estimates. With a mass estimate of the UAV being around 8.5 kg, the propulsion system needs to be designed such that it sustains the UAV in different phases of flight. Typically, UAVs used for aerial photography or reconnaissance missions require a thrust to weight ratio of 1.5. Considering this, the propulsion system must produce a thrust of 13 kg or 48 N (acceleration due to gravity on Mars being 3.7 m/s^2).

Next, the velocities in the transonic regime must be avoided to prevent the effects of shock waves, which can lead to increase in drag and possible structural damage. The rotor speed is influenced by three major factors: hover tip Mach number, advancing blade tip Mach number and tip speed ratio which are limited to Mach 0.7, Mach 0.88 and 0.4, respectively. The three limitations when plotted together can be called as the Constraint Diagram. The constraint diagram gives two design points A and B, as shown in Figure 5.1. Since getting the maximum thrust force is a priority, point A was chosen as the Design Point. Thus, the maximum rotational or tip velocity and the maximum forward velocity are,

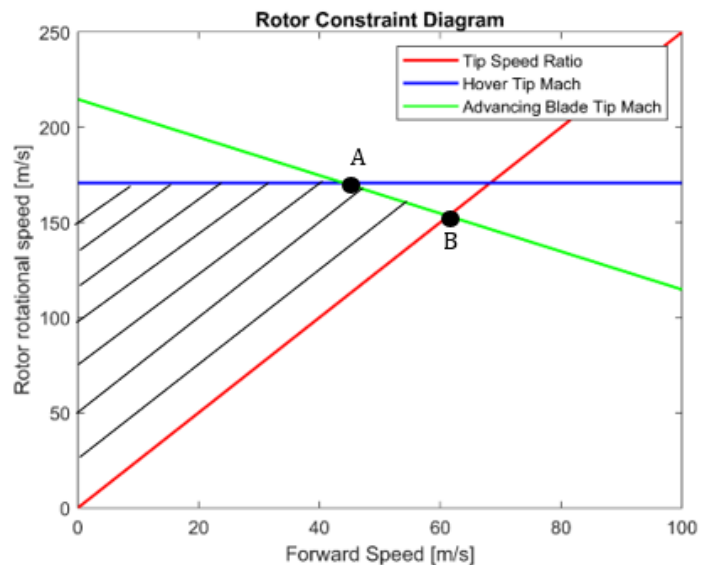


Figure 5.1: Rotor Constraint Diagram

$$V_{tip} = 171 \text{ m/s} \quad [5.1]$$

$$V_{forward} = 42 \text{ m/s} \quad [5.2]$$

The blade tip velocity is the product of angular velocity and the blade radius. Thus, for varying radii, the limiting revolutions per minute (RPM) can be obtained.

By assuming the power consumption by the rotor based on commercially available UAVs, the radius of the rotor is calculated. The lift produced by the aerofoil plays a significant role in designing a blade and thus, high lift aerofoils were chosen. The blade loading coefficient was estimated using the lift coefficient of the chosen aerofoil. Thence, the blade area, chord, solidity and pitch angles at the root and at the tip were estimated. A detailed procedure of the initial sizing is provided in the Appendix B (BEMT).

With these initial data, Blade Element Momentum Theory (BEMT) was used to calculate the thrust, torque and power consumed per rotor. XFOIL application was incorporated into the code. The code was an adaption of two programs from an online resource [10] [11].

The two programs were modified to suit the requirements and output. The work flow is described in the flowchart shown in Figure 5.2. The code was validated against real-world helicopters by comparing the gross take-off mass and the error was found to be 2 – 8%.

Several combinations of different values of the initial data were tried out. The first airfoil considered was the Clark Y. Subsequently, Eppler 423 (E423), Selig 1223 (S1223) and a hybrid between Eppler 423 and S1223 were also considered. The outputs of the code are thrust, torque and power consumed per rotor. The most suitable values of the blade parameters are shown in Table 5.1 and outputs for different airfoil are shown in Table 5.2. Since the Eppler 423 and the S1223 airfoil gave the highest thrust values compared to other airfoil, the CFD analyses were run for the two airfoil.

Radius [m]	Tip chord [m]	Root chord [m]	Tip pitch [°]	Root pitch [°]
0.7	0.07	0.2	10	14

Parameters	Clark Y	Eppler 423	S1223	Hybrid
Power [W]	170	275	311	308
Thrust per rotor [N]	5.24	8.64	12.93	12.96
Total Thrust [N]	22.78	34.51	51.72	51.84
Torque [Nm]	0.70	1.14	1.30	1.30

To fulfil the requirements of the propulsion system, two coaxial rotor configurations was chosen. Totally, the UAV would have four rotors, two on either side. The two rotors on each side are contra-rotating to reduce the effect of the torque generated. Thus, the total thrust in Table 5.2 shows the thrust due to four rotors.

It can be seen from Table 5.2 that Selig 1223 and Hybrid models provide the highest thrust values. In order to choose one of them, structural analyses of the two models were performed to investigate their structural strengths.

5.2. Computational Fluid Dynamics

During the design of the UAV system, computational fluid dynamics (CFD) was utilized to evaluate how much thrust is produced by one rotor for both the propellers. The results were then validated with the results from the analytical solution. All simulations were performed under steady state conditions with Ansys Fluent. For the analysis, only one propeller (consisting of 3 blades and hub) was considered to make the analysis simple. The details on the method, meshing and mesh independence are provided in the Appendix A (CFD).

5.2.1. Results/Validation

The results from the simulations are compared with the analytical solution as shown in Table 5.3 to validate the results. As seen in Table 5.3, the thrust is under-predicted in the CFD results for both the rotors, although it is slightly higher for S1223. The under-prediction could possibly be due to small simplifications made to the propeller geometry since the thrust is dependent on the shape of the propeller airfoil. The torque is slightly higher than analytical in both cases, which could possibly be due to the mesh and the discretization scheme used while solving.

Parameters	Analytical (S1223)	CFD (S1223)	Analytical (Hybrid)	CFD (Hybrid)
Thrust (N) (per rotor)	12.93	11.36	12.96	11.13
Torque (Nm)	1.3	1.6	1.3	1.9

Velocity distribution around the rotor

The velocity field is studied with the help of streamlines coloured by velocity as shown in Figure 5.2. As seen from Figure 5.2, the velocity streamlines, move in a radially outward direction and have a value of close to 146 m/s closer to the tip. Based on the freestream velocity of 244 m/s on Mars, the Mach number at the tip is about 0.59 which shows that the blade is not prone to compressibility effects.

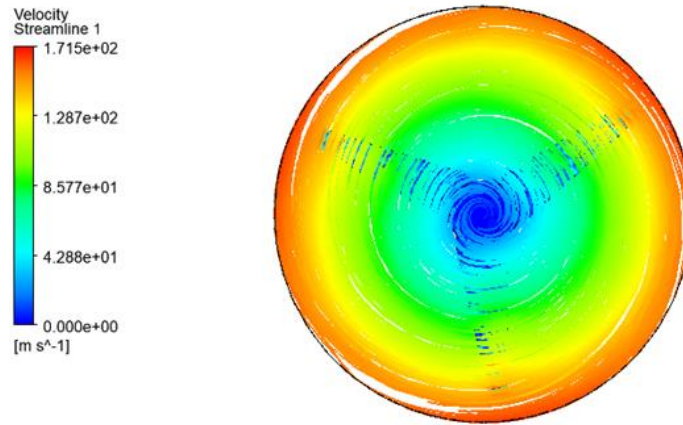


Figure 5.2: Streamline velocities around the propeller.

From the CFD study, it can be concluded that the thrust produced by the rotor is lower. But considering that there are simplifications made in CFD and it is only an approximate of the actual operating conditions, it can be concluded that the rotor performance is satisfactory to produce the required thrust. Although the torque is slightly higher in CFD and can affect the performance of the motor, the actual effect can be understood only when the motor is working under actual Martian conditions. Based on the CFD results, structural analysis is carried out to finalise the propeller choice.

5.3. Structural Analyses

The Hybrid and the Selig 1223 models give similar thrust, the structural strength of the models would be the deciding factor for the airfoil selection. The input for the blades were the pressure loads from CFD and rotational velocity of 209 rad/s (clockwise). The Carbon fibre Woven blade results were monitored for vertical deflection, minimum principal stress and normal stress in the Z – direction. The Z – direction normal stresses were monitored since the tensile and compressive strengths of the composite are the least out of all the directional strengths.

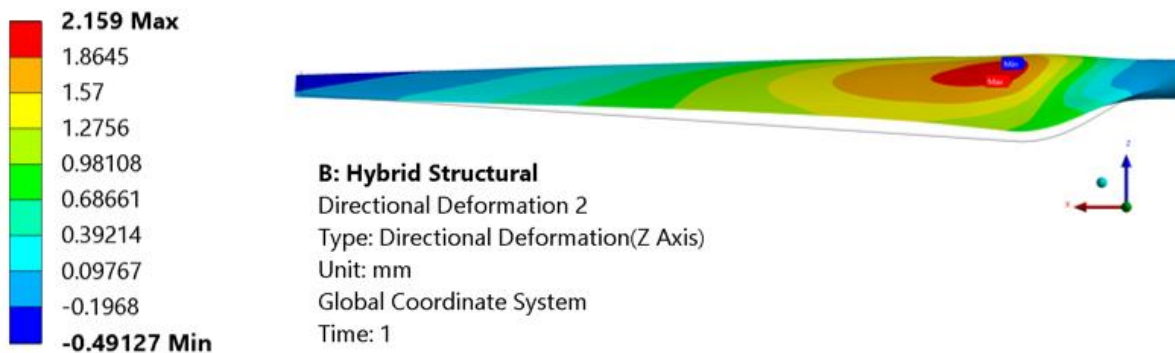


Figure 5.3: Directional Deformation in Z – axis for Hybrid model

Comparing S1223 and Hybrid deformation, the root of the blade has a directional deformation of 2.15 mm in hybrid (Figure 5.3) and 2.76 mm in S1223 (Figure 5.4). However, the S1223 has a maximum deformation at the tip of 5.3mm while the Hybrid has about 1.78 mm. This is because of the presence of E423 airfoil section at the root of the hybrid which has higher stiffness due to larger thickness of the airfoil and higher maximum principal stress is seen near the root section. Though the normal stresses in X- and Y- directions do not exceed the limiting strengths, the normal stress in Z – direction reaches about 62 MPa (Figure 5.5) which can be avoided by adding reinforcements or filler airloy foam.

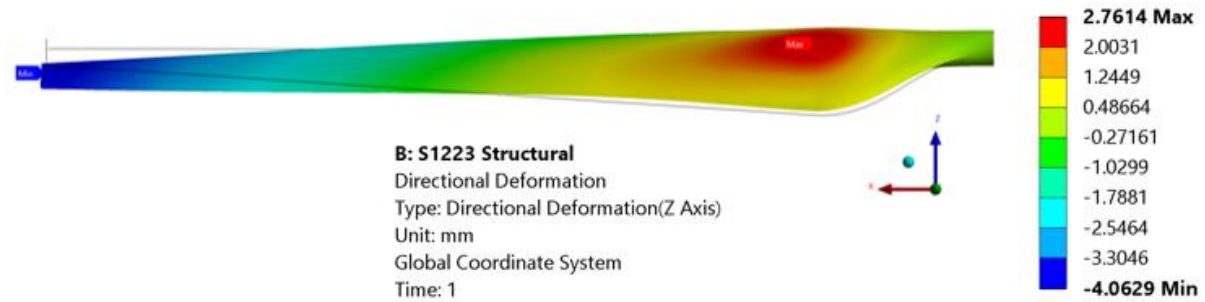


Figure 5.4: Directional Deformation in Z – axis for S1223 model

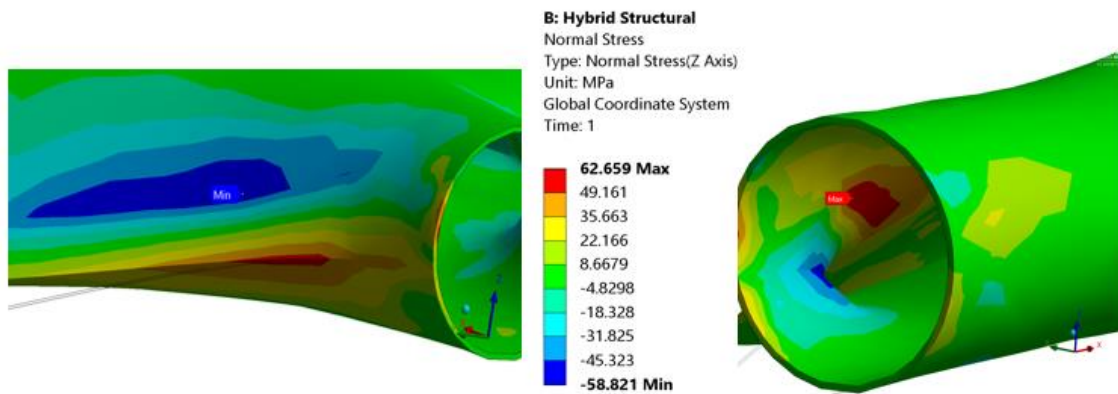


Figure 5.5: Normal Stress in Z – direction for Hybrid Model

5.4. Final Geometry

To encapsulate, S1223 and a Hybrid rotor were considered as two possible choices for the propulsion system. From CFD and structural analyses, it was concluded that Hybrid blade was found to be a better choice due to its high thrust as well as high structural stiffness. The final blade design is shown in Figure 5.6.



Figure 5.6(a)



Figure 5.6(b)

Figure 5.6: Final Blade Geometry

5.5. Swash Plate



Figure 5.7(a)

Figure 5.7(b)

Figure 5.7: Swash Plate

From the initial blade design, it was calculated that the range pitch angle is +15 degree and - 15 degree from the mean position. So, the swash plate is designed to achieve the intended cyclic pitch. The design of the swash plate for the coaxial rotors is made individually so, as to vary the pitch individually and provide better control. As shown in Figure 5.7, Graphalloy is used as solid lubricator between the upper and lower swash plates due to distinct cryogenic applications. The bottom rotor's swash plate is designed to prevent the plates from falling using weight and the propeller shaft support.

6. Structures

6.1. Frame

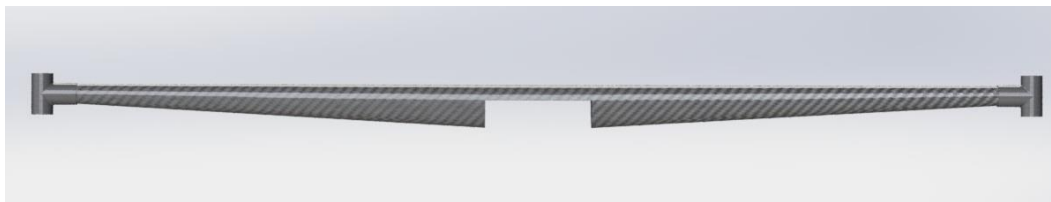


Figure 6.1: UAV Frame

The frame is a sandwich composite beam with 4 layers (0,45,45,0) of 0.76 mm thick Woven Carbon Fiber, 1 layer of 1 mm thick Glass Fibre and a 1mm thick beam of Aluminium 7075 - T6, at the core. The circular cross section is chosen for the ease of fittings at the rotor ends, greater resistance to twisting moments and aerodynamic profile between the rotors. The cross section towards the centre portion of the frame is blended into an ellipse to provide better bending strength for the frame. From the structural analysis, it is found that the max deflection due to weights of the rotor and the thrust provided by them, are within the limits (vertical clearance between the rotors), as shown in the Figure 6.2.

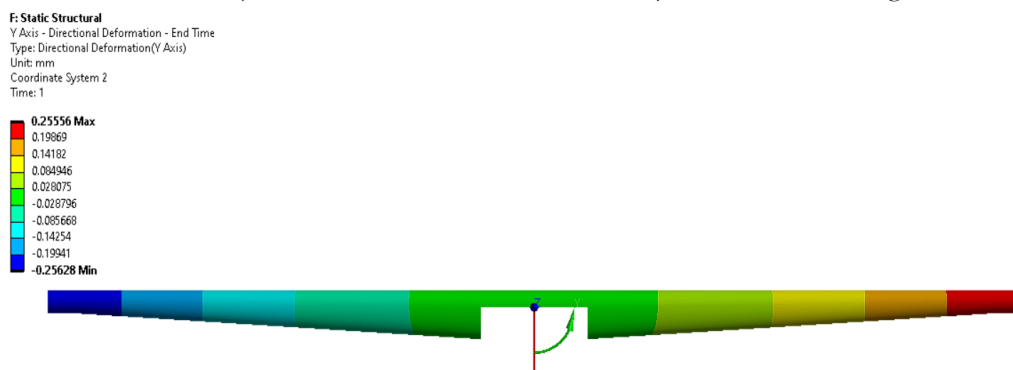


Figure 6.2: Directional deformation of frame structure in Y – axis

6.2. Pickup mechanism of UAV

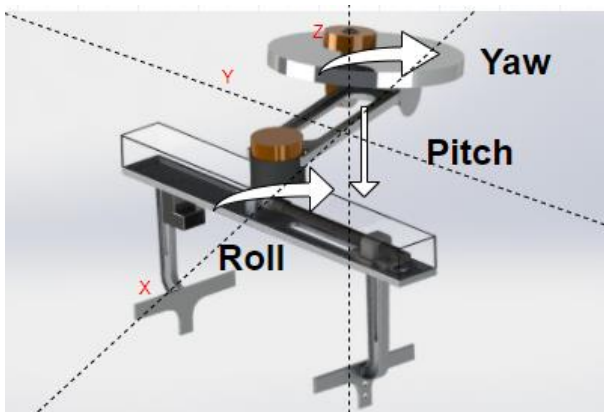


Figure 6.3

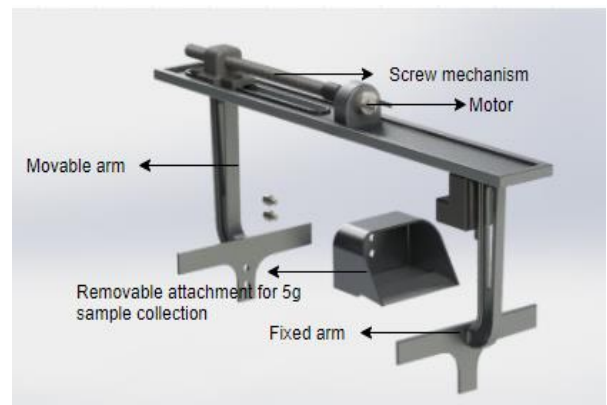


Figure 6.3 (b)

Figure 6.3: (a) and (b) Represents the Pickup Mechanism and its Degrees of Freedom

In the above Figure 6.3(a) shows the Pickup mechanism depicting the of the mechanism in X, Y, Z direction and Figure 6.3(b) shows the Gripper of the robotic arm of the pickup mechanism is accommodated with a detachable spoon that can be used for 5g soil sample collection. The screw sliding mechanism slides in with the help of a motor to carry the 15x15x15 cm package. A sensor is placed at the two arms of the gripper to sense the holding of the package.

7. Epilogue

UAVs as observers in the sky will remain important for the indefinite future. They will grow easier to operate. The Autonomous capability of our Mars UAV of flying and taking pictures, analysing atmospheric data and ability to pick up/drop packages can mask the fact that questions concerning how to use the Avionics system will not get any easier with higher sensor resolutions, better lenses, or cheaper memory. Large companies like Amazon and Google propose to reshape the rich world's infrastructure with drones delivering packages that are now sent by truck. Many of these cargo initiatives plan on aircraft that will take off vertically and fly horizontally. This is a technically tricky problem we tried to solve in our UAV. The Avionics system is a necessary hump to be overcome if delivery drones are to prove economically viable for exploration on Mars. Pure quadcopters lack the needed range and endurance, fixed-wing aircraft that can carry a substantial payload need too much space to take off and land. But if our package delivery UAV succeeds, it will likely far outnumber all the other uses of drones put together.

On the utilization of new UAV system technology “How are we to live together? How can we live gracefully and with justice?” These may seem rather generic questions to pose in closing a Avionics chapter of our Mars UAV. However, the hope expressed in this EDR is that the information that UAV can gather in some small way will help answer the Mars astronauts initiating the Autonomous UAV.

8. Future Advancements

To furthermore automation from level 4 UAV to control tune into fully automatic level 5 UAV, we tend to incorporate the following features which will in return help humanity to explore the Martian terrain.

- 1) CIFER - Comprehensive Identification from frequency to detect Extra-terrestrial Life (Aliens)
- 2) AHRS - An Attitude and Heading Reference System
- 3) Voice Controlled FPV Goggles Man Machine Interface
- 4) UAV Data Encryption
- 5) LASER SWARM Operation & Communication
- 6) Electrical Insulators for Motors & Battery for Martian Nights
- 7) Aerial Battery Exchange Base Station
- 8) AI Based Trajectory Optimization

The propulsion system can be worked upon to find ways to augment the thrust produced by the rotors by improvements in blade geometry.

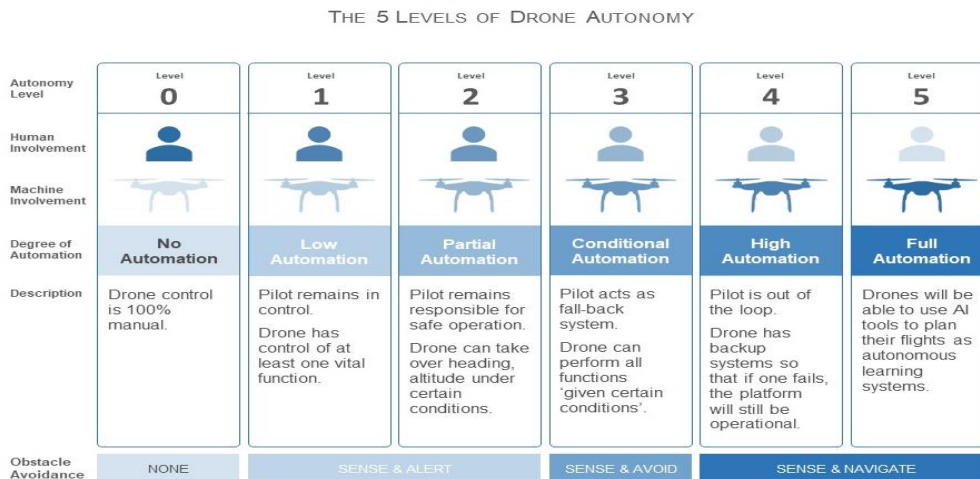


Figure 7.1: Drone Autonomy

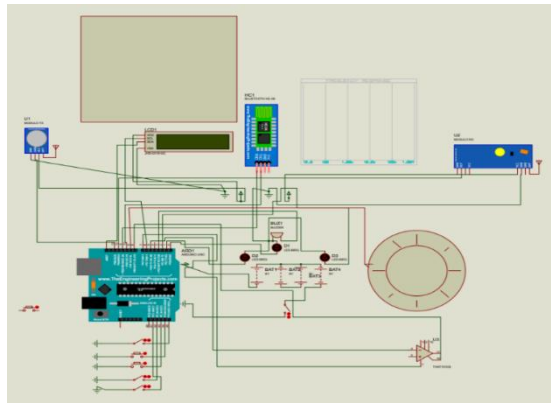


Figure 7.2

9. References

[1]	Soil on Mars. URL http://tomatosphere.letstalkscience.ca/Resources/library/ArticleId/5302/soil-on-mars.aspx
[2]	Martian Soil. URL https://en.wikipedia.org/wiki/Martian_soil
[3]	Composition of Mars. URL https://en.wikipedia.org/wiki/Composition_of_Mars
[4]	What is Mars made of. URL https://www.space.com/16895-what-is-mars-made-of.html
[5]	Marsquake. URL https://en.wikipedia.org/wiki/Marsquake
[6]	https://agupubs.onlinelibrary.wiley.com/doi/full/10.1029/2018JE005854 , http://sprg.ssl.berkeley.edu/~rillis/Mars_crustal_field/ Ingest date: 5/10/20
[7]	http://pds-geosciences.wustl.edu/missions/mgs/mola.html .
[8]	[Reference - Unmanned Aerial Vehicles (UAVs): Collision Avoidance Systems and Approaches (IEEE)]
[9]	[F Sani, Moe & Karimian, Ghader. (2017). Automatic navigation and landing of an indoor AR. drone quadrotor using ArUco marker and inertial sensors. 102-107. 10.1109/ICONDA.2017.8270408.]
[10]	Running XFoil from MATLAB. URL https://www.joshtheengineer.com/2019/01/30/running-xfoil-from-matlab/
[11]	Blade Element Propeller Theory. URL http://www.aerodynamics4students.com/propulsion/blade-element-rotor-theory.php

A. APPENDIX – CFD

Method

The CAD model of the propeller was first created with CATIA V5. This was done by importing the airfoil details and then creating the required propeller profile. This geometry was simplified to ensure compatibility with the CFD software. For instance, the shaft hole for the propeller is made solid, sharp edges and corners are smoothed on the airfoil and the hub is made thicker.

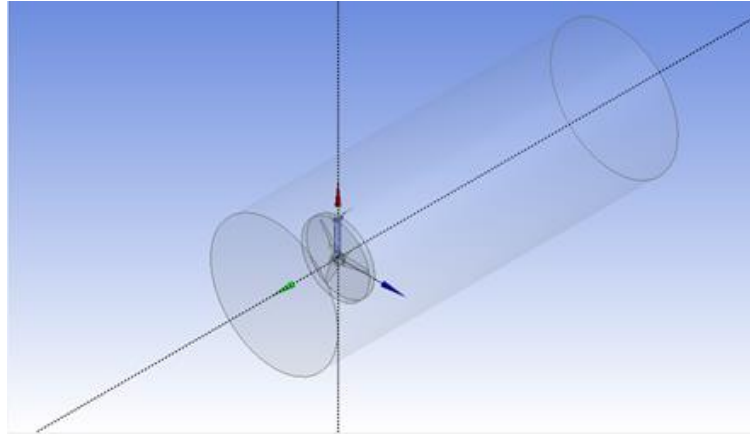


Figure A1(a)

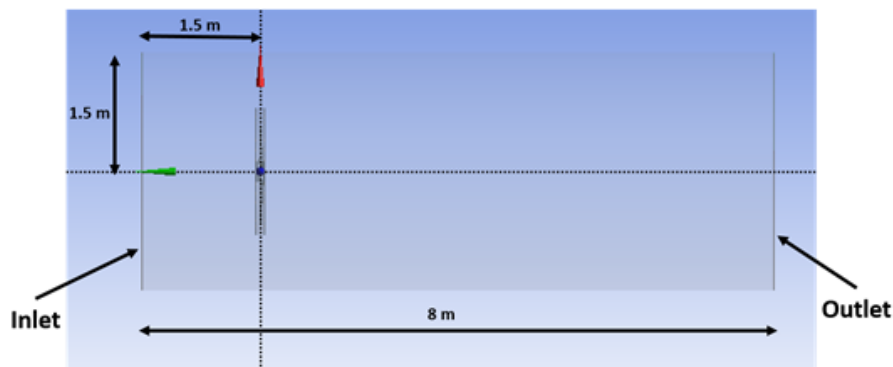


Figure A1(b)

Figure A1: Geometry of the computational domain with the propeller.

After importing the CAD model of the propeller into the simulation software, the computational domain was created. The computational domain represents the region inside which the CFD simulations are carried out. The domain as shown in Figure 1, was selected to be cylindrical in shape with a radius of 1.5 m and length of 8 m. The inlet to the domain was positioned at 1.5 m from the propeller and the outlet at placed 6 m behind the propeller. The outlet is positioned sufficiently far away to enable development of the flow behind the propeller. This domain was labelled as the static domain. Since the propeller is not rotating in this case as it is a steady state simulation, the mesh around the propeller is defined with a rotational velocity. For this purpose, around the propeller, another body was created to mimic the propeller rotation and was labelled as the rotating domain.

Meshing

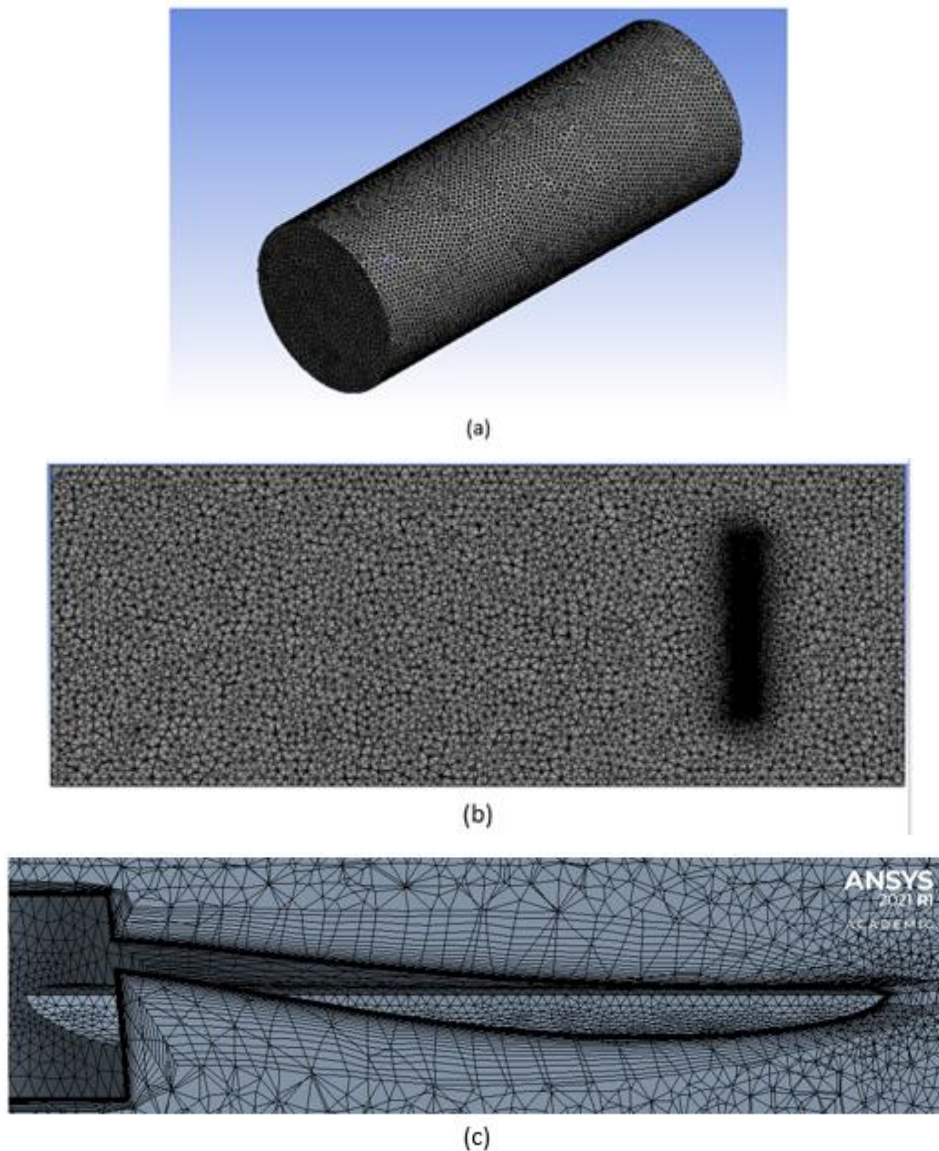


Figure A2: Representation of the mesh on (a) the domain (b) cut section plane at the centre of the domain (c) near the propeller highlighting the inflation layers.

After creating the domain, the CAD model along with the domain was meshed. To carry out meshing, the static domain was first defined with a face sizing on all faces. Similarly, face sizing was defined on the rotating domain for a smaller element size. The overall mesh is shown in Figure A2(a). In the regions around the propeller, inflation layers were added to capture the flow physics better. The first layer height was calculated based on the free stream velocity and density of flow and was obtained as $1\text{E-}6$ m. Suitable number of inflation layers were added as shown in Figure A2(b). As seen in Figure A2(b), the transition between the different element types in the inflation layers and the global mesh is controlled with the help of growth rate and maximum element size to have a smooth transition between elements of different sizes.

Mesh independence study

To ensure that the final solution is independent of the mesh chosen, a mesh independence study was carried out as shown in Table A1. The study was started with a coarse mesh and then the number of elements around the propeller was doubled between the next two meshes. It is observed from the results of the mesh study that the thrust increases as the mesh is refined and the percentage change in the thrust between the last two meshes is about 0.2 %. At this point, the solution can be considered independent of the mesh. Although a mesh with 10L elements would give slightly better results, in order to save computational time, the mesh with 490000 elements is chosen as the final mesh.

Table A1: Results from mesh independence study.

No. of elements	Thrust [N]	Percentage error [%]
125199	9.93	-
250000	10.84	9.1
490000	11.13	2.6
10,00,000	11.15	0.2

Boundary conditions and setup

Standard aerodynamic boundary conditions were defined to carry out the CFD simulations. The boundary conditions are shown in Table A2. The inlet where the flow enters the domain was defined as a velocity inlet with a velocity of 5 m/s. The outlet of the domain was set as a pressure outlet. All other regions were defined as no-slip walls.

Table A2: Boundary conditions for the computational domain		
Region	Boundary type	Value
Inlet	Velocity Inlet	5 m/s
Outlet	Pressure Outlet	0 Pa
Rotating domain	Rotating wall	2000 rpm

All simulations were performed under steady state conditions with a SST $k - \omega$ turbulence model under Martian conditions. The operating conditions namely the density, pressure and viscosity of air on Mars along with the gravity were defined as shown in Table A3. All simulations were run for 3000 iterations and observed for convergence. Along with the scaled residuals plot, the thrust produced by the propeller was also monitored.

Table A3: Operating conditions on Mars.	
Property	Value
Density [kg/m ³]	0.0167
Dynamic viscosity [Ns/m]	9.82E-6
Gravity [m/s ²]	3.7
Pressure [Pa]	644

B. APPENDIX – BEMT

The equations used in the initial sizing are provided below.

$$\omega = 2 \times \rho \times \left(\frac{P_i}{Wr} \right)^2 \quad [8.1]$$

$$R = \sqrt{\frac{Wr}{\pi \omega}} \quad [8.2]$$

$$Re = \frac{\rho V c}{\mu} \quad [8.3]$$

$$C_T / \sigma = \bar{C}_L / 6 \quad [8.4]$$

$$NcR = \frac{Wr / \rho \times (\Omega R)^2}{C_T / \sigma} \quad [8.5]$$

$$c = \frac{NcR}{\pi R} \quad [8.6]$$

$$\theta = \frac{6}{\sigma a} C_T + \frac{3}{2} \sqrt{\frac{C_T}{2}} \quad [8.7]$$

where,

ω is disk loading, kg/m^2

ρ is density on Mars, kg/m^3

P_i is induced power, W

Wr is mass lifted per rotor, kg

R is rotor radius, m

Re is Reynold's number of the blade,

V is blade rotational speed, m/s

c is blade chord length, m

μ is dynamic viscosity on Mars, Ns/m

C_T is thrust coefficient,

σ is blade solidity,

\bar{C}_L is total blade lift coefficient

C_T / σ blade loading coefficient,

NcR is blade area, m^2

πR is disk area, m^2

Ω is angular velocity, rad/s

a is lift curve slope of an airfoil, rad^{-1}

θ is blade pitch angle, $radians$.

The BEMT code was run after the initial sizing performed using the Equations [8.1 – 8.7]. Figure B1 shows the flowchart of the code used to run the blade element theory. The parameter used to check for convergence was the induced velocity and was set to 1E-5.

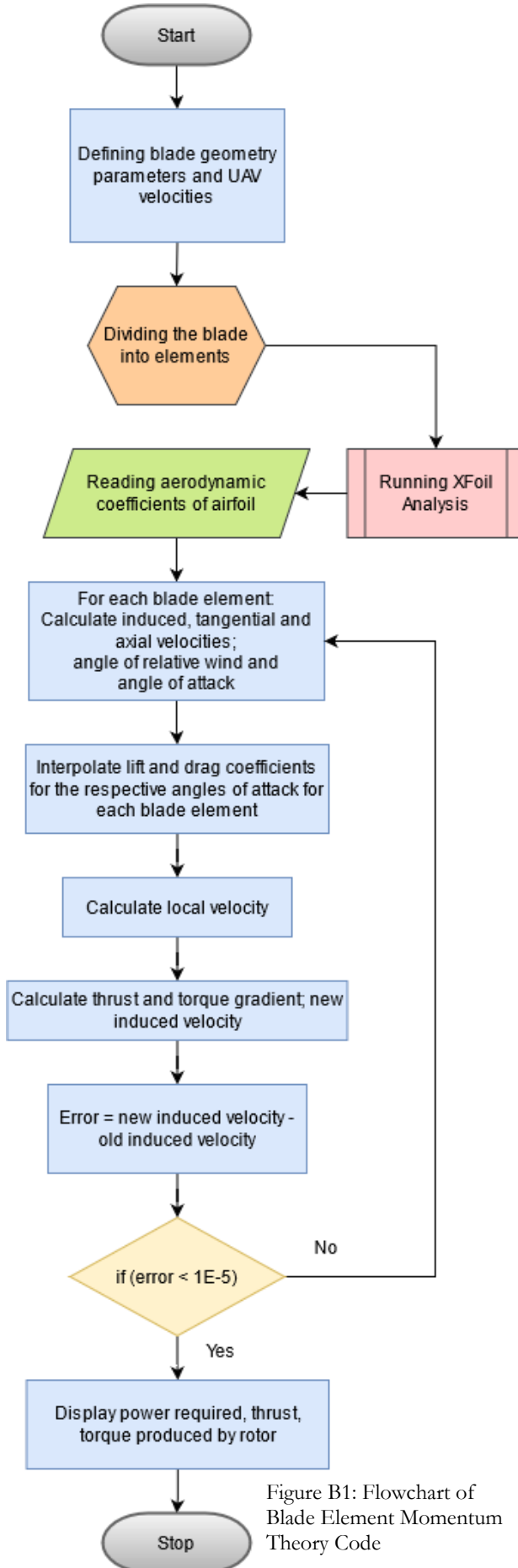


Figure B1: Flowchart of Blade Element Momentum Theory Code

C. APPENDIX – MATERIALS

Table C1: Titanium Alloy Material Properties	
Material	Ti6Al4V Grade 5
Shear Strength [MPa]	550 MPa
Yield strength	≥ 828 MPa
Young's modulus	105-120 GPa
Poisson ratio	0.31
Density	4.43 g/cm ³
Tensile strength	≥ 895 MPa
Thermal expansion co-efficient (@0.000-100°C/32-212°F)	9 μm/m°C
Thermal conductivity k	6.60W/mK
Shear modulus	41-45 GPa

Materials	Density (Kg/m ³)	Ultimate Strength (T) MPa	Yield Strength (T) MPa	Modulus of Elasticity GPa
Al 7075-T6	2800	570	500	72

	Boron Epoxy	Nomex	Aerogel	Martian Air
Density (kg/m ³)	1740	48	3	0.02
Thickness (m)	0.003	0.006	0.02	-
Thermal Conductivity (W/mK)	0.57	0.37	0.017	-
Convective Heat Transfer Coefficient (W/m ² K)	-	-	-	460.24

Composites	Density [kg/m ³]	Young's modulus X [Pa]	Young's modulus Y [Pa]	Young's modulus Z [Pa]	Poisson XY	Poisson YZ	Poisson XZ
Epoxy Carbon UD (395 GPa) Prepreg	1540	209E9	9.45E9	9.45E9	0.27	0.4	0.27
Epoxy Carbon Woven (395 GPa) Prepreg	1480	91.82E9	9.182E9	9.00E9	0.05	0.3	0.3
Boron Epoxy	1740	30.3E6	1.80E6	1.80E6	0.25	0.25	0.25

Composites	Shear Modulus XY [Pa]	Shear Modulus YZ [Pa]	Shear Modulus XZ [Pa]	Thermal Conductivity (X) [-]	Thermal Conductivity (Y) [-]	Thermal Conductivity (Z) [-]	α
Epoxy Carbon UD (395 GPa) Prepreg	5.5E9	5.5E9	5.5E9	5 – 7	0.5 – 0.8	0.5 – 0.8	0.1E-6
Epoxy Carbon Woven (395 GPa) Prepreg	3.6E9	3.0E9	3.0E9	5 – 7	5 – 7	0.5 – 0.8	-
Boron Epoxy	0.57	-	-	-	-	-	-

α – Coefficient of Thermal Expansion,

[-] The data cell left empty signifies the unavailability of value on opensource forums.

D. APPENDIX – MATERIALS

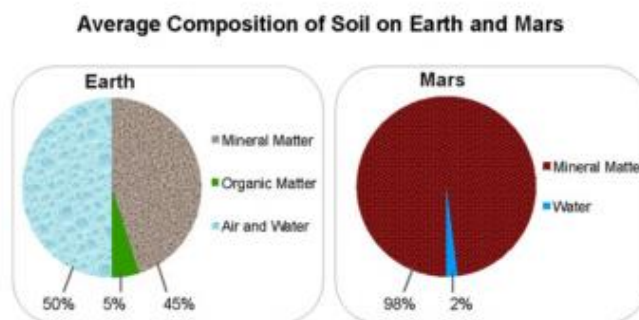
Section D1:

Element	Pathfinder A-2, Soil ^[5]	Pathfinder A-4, Soil ^[5]	Pathfinder A-5, Soil ^[5]	Viking 1 Lander Site ^[6]
	Weight %	Weight %	Weight %	Weight %
Carbon [C]	-	-	-	-
Oxygen [O]	42.5	43.9	43.2	-
Sodium [Na]	3.2	3.8	2.6	-
Magnesium [Mg]	5.3	5.5	5.2	5.0 +/- 2.5
Aluminum [Al]	4.2	5.5	5.4	3.0 +/- 0.9
Silicon [Si]	21.6	20.2	20.5	20.9 +/- 2.5
Phosphorus [P]	-	1.5	1.0	-
Sulfur [S]	1.7	2.5	2.2	3.1 +/- 0.5
Chlorine [Cl]	-	0.6	0.6	0.7 +/- 0.3
Potassium [K]	0.5	0.6	0.6	< 0.25
Calcium [Ca]	4.5	3.4	3.8	4.0 +/- 0.8
Titanium [Ti]	0.6	0.7	0.4	0.5 +/- 0.2
Chromium [Cr]	0.2	0.3	0.3	-
Manganese [Mn]	0.4	0.4	0.5	-
Iron [Fe]	15.2	11.2	13.6	12.7 +/- 2.0
Nickel [Ni]	-	-	0.1	-
Not Directly Detected*	-	-	-	50.1 +/- 4.3
Sum	100	100	100	49.9

* Includes H₂O, NaO, CO₂, NO_x, and trace amounts of Rb, Sr, Y and Zr



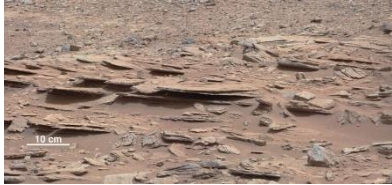
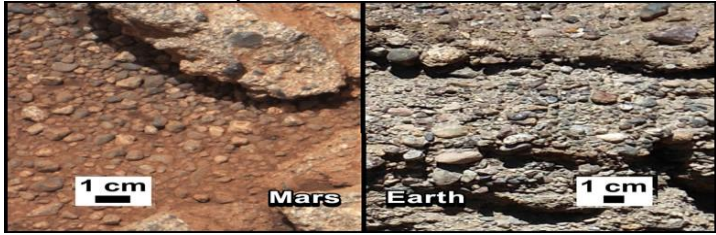
Table D1: Elemental composition of Martian soil

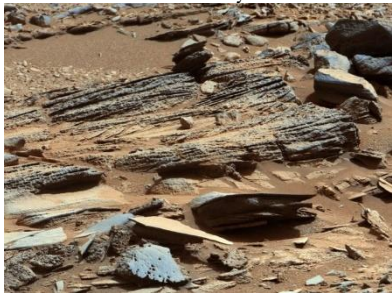



Ref: <https://agupubs.onlinelibrary.wiley.com/doi/pdfdirect/10.1029/1999GL008432>



Ref: <http://tomatosphere.letstalkscience.ca/Resources/library/ArticleId/5302/soil-on-mars.aspx>

Section D2:

Table D2: Various features studied for site selection		
Rocks	Captured by	Composition or Relevance
Mudstone	Mars Curiosity Rover 2015 at Gale Crater 	The crater contains thick deposits of finely laminated mudstone that represent fine-grained sediments deposited in a standing body of water that persisted for a long period of time - long enough to allow sediments to accumulate to significant thickness.
Sandstone	Mars Rover Curiosity at lower slope of Mars Mount Sharp 	It shows an outcrop of cross-bedded sandstone.
Shale	Mars Rover Curiosity in 2012 at Gale Crater 	They are fine-grained, thinly layered and fissile (meaning they easily break into thin sheets). Their plate-shaped grains deposited on the bottom in a parallel orientation. This gives the rock the ability to be split into thin layers. Clay minerals are known to be abundant on Mars, so it is likely that these rocks are composed of clay minerals.
Conglomerate	Mars Rover Curiosity in 2012 	The presence of conglomerate and sandstones on Mars is evidence of moving water. Wind is not strong enough to pick up pebbles over one centimeter in diameter and carry them along in the current. The pebbles in this rock show a high

		level of rounding which implies a significant distance of transport. The red color is thought to be iron staining, which is nearly ubiquitous on Mars and gives it the name "Red Planet." The "cement" that binds the particles in these rocks could be a sulfate mineral
Cross Bedding	Mars Rover Curiosity in 2012 at Gale crater 	Multiple angles of cross bedding reveal that the direction of wind or water flow changed over time.
Columnar Basalt	Mars Reconnaissance Orbiter near Marte Vallis. 	It shows an outcrop of a <u>basalt</u> flow with columnar jointing.
Meteorite	Mars Exploration Rover Opportunity in 2005. 	The first <u>meteorite</u> ever discovered on the surface of another planet. It is a baseball-size <u>iron-nickel meteorite</u> . The Mars meteorites also display very little surface alteration. This confirms that the atmosphere and surface soil of Mars contain very little moisture or free oxygen.
Scoria	Spirit Rover 	The rock has a rough surface and vesicles
Sand Dunes	Mars Reconnaissance Orbiter in 2015	

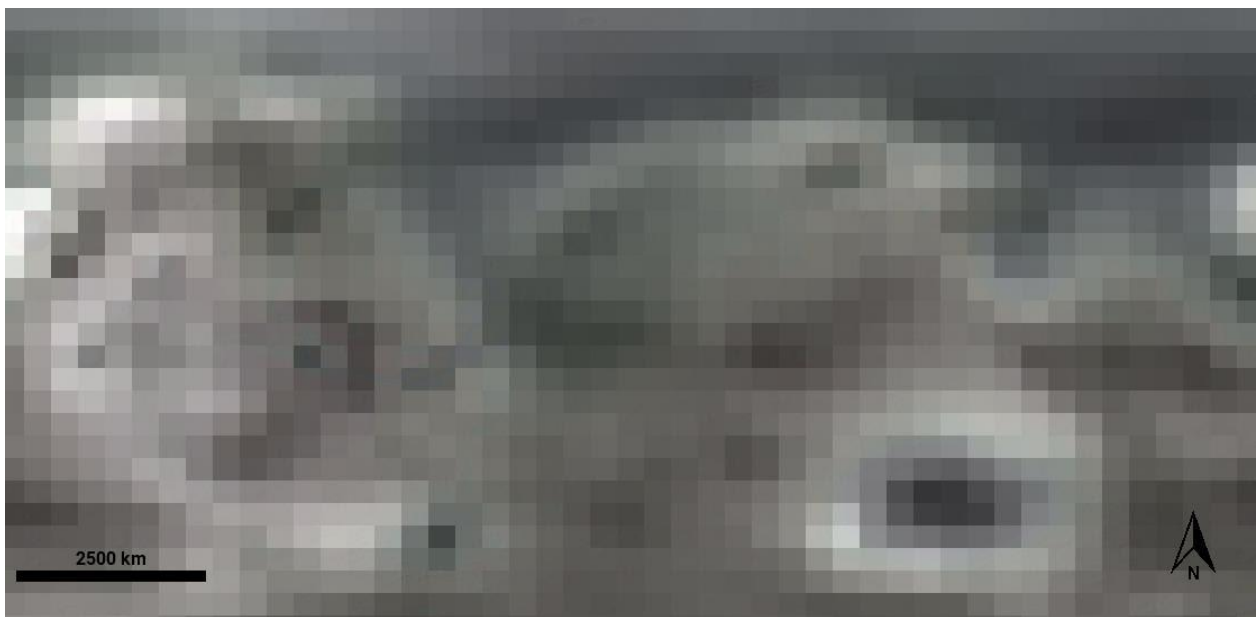


Section D3:

Life on Mars and Evidences

- NASA Viking Lander 1976 performed three experiments namely Gas exchange experiment, Labelled released experiment and a pyrolytic release experiment. Only label release experiments came out with positive results.
- Martian meteorite — Allan Hills 84001 fell on Earth around 13000 years ago and was found to contain the minerals that are possible suspects of remnants of fossilized organic life forms.
- Mars rover: Curiosity found that there are underground methane hotspots that arise during spring and end of winter seasons on Mars. This is quite uncertain because this can be caused by organic, inorganic and geochemical processes due to seasonal change.

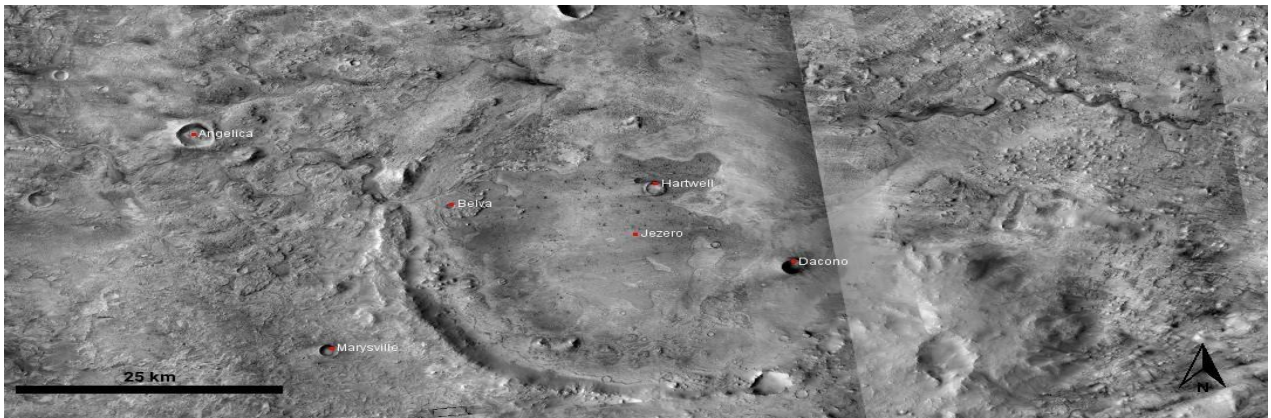
Section D4:



Dust storm map of entire mars created in JMARS GIS. Regions in white experience higher dust storms. However, dust storm cycles are experienced in three categories: regional, seasonal and global. And this map shows the global average.



Fig: This is the albedo map of Mars. Regions with higher albedo have greater drop in temperature and are less preferred for landing site selection.
 Jezero Crater figure



Weathering clay sequence marked around jezero. Mars Reconnaissance Orbiter's CRISM instrument's data helps scientists predict clay deposits at and around Jezero which could only be present as a result of water. This makes Jezero crater an important landing site for scientific research exploration.



Martian magnetic field B magnitude in nanotesla at 130 km altitude, as calculated using a spherical harmonic representation (up to $n, m=134$), of an equivalent source dipole model of Mars' internal (i.e. crustal) magnetic field by Langlais et al. [JGR, 2018], constrained using data from three instruments: (a) Mars Global Surveyor (MGS) magnetometer (1997–2006), (b) MGS Electron Reflectometer (1999–2006), and (c) Mars Atmosphere and Volatile EvolutionN (MAVEN) magnetometer (2014 to 2018)-
<https://agupubs.onlinelibrary.wiley.com/doi/full/10.1029/2018JE005854>,
http://sprg.ssl.berkeley.edu/~rlillis/Mars_crustal_field/ Ingest date: 5/10/20
 [7]This Mars Orbiter Laser Altimeter (MOLA) instrument colorized shaded relief data layer is derived from Planetary Data System source images at <http://pds-geosciences.wustl.edu/missions/mgs/mola.html>. This data product is a shape map of Mars at a resolution of 0.00781 (1/128) by 0.00781 degrees, based on altimetry data acquired by the Mars Global Surveyor MOLA instrument and accumulated over the course of the primary and extended mission.